

Configurational-entropy-driven structural and optical stability in high-entropy halide perovskites for broadband NIR photonics

Yuxiang Xin[†], Chen-Xin Yu[†], Jianru Wang, Shuwen Yan, Liang Fan, Xiachu, Xiao, Yutao, Yang, Luying, Li, Jiang, Tang, Li-Ming Yang^{*} and Zhuolei Zhang^{*}

[*] Y. Xin, C. Yu, J. Wang, L. Fan, X., Xiao, Y., Yang, L. Yang, Z. Zhang

School of Chemistry and Chemical Engineering, Hubei Key Laboratory of Bioinorganic Chemistry and Materia Medica, Hubei Engineering Research Center for Biomaterials and Medical Protective Materials, Key Laboratory of Material Chemistry for Energy Conversion and Storage, Ministry of Education, Huazhong University of Science and Technology (HUST), Wuhan 430074, P. R. China

E-mail: zzhuolei@hust.edu.cn; Lmyang@hust.edu.cn

Y. Xin, J. Wang, L. Fan, X., Xiao, Y., Yang, Z. Zhang

Guangdong HUST (Huazhong University of Science and Technology) Industrial Technology Research Institute Dongguan 523808, P.R. China

S. Yan, L. Li, J. Tang

Wuhan National Laboratory for Optoelectronics (WNLO) and School of Optical and Electronic Information, Huazhong University of Science and Technology (HUST), 1037 Luoyu Road, Wuhan, Hubei 430074, China

[†] These authors contributed equally to this work.

Abstract

By injecting configurational entropy into soft ionic frameworks, high-entropy halide perovskites redefine what is possible for stable photonic materials; however, how to turn compositional complexity into predictable optical function remains a key frontier. Here we show that compositional complexity can be converted into device-relevant ultrabroadband near-infrared (NIR) photonics by integrating element-specific roles within one entropy-stabilized lattice. We establish entropy-engineered rare-earth halide double perovskite single crystals, $\text{Cs}_2\text{Na}(\text{Sb, Re})\text{Cl}_6$ ($\text{Re}^{3+} = \text{Sc}^{3+}, \text{Er}^{3+}, \text{Yb}^{3+}, \text{Tm}^{3+}$), in which near-equatomic B(III)-site alloying yields a single-phase high-entropy solid solution ($\Delta S_{\text{config}} \approx 1.6R$) with homogeneous multication incorporation. Sb^{3+} serves as a broadband sensitizer to unify excitation and cooperatively activate multiple lanthanide emitters, transforming the parent single-mode emission into a wide-coverage NIR output spanning ~ 850 – 1600 nm with three spectrally separated fingerprint bands at 996, 1220, and 1540 nm. The resulting tri-peak, self-referenced signature enables redundancy-based ratiometric analysis with reduced sensitivity to intensity drift, allowing reliable solvent identification and quantitative mixture sensing. Beyond functional expansion, accelerated aging tests reveal markedly enhanced tolerance to humidity and oxygen relative to single-component analogues. This robustness is experimentally rationalized by octahedral contraction–strengthened metal–halide bonding that raises the kinetic barrier for moisture-triggered bond cleavage, together with entropy-induced lattice distortion that impedes long-range halide migration and suppresses defect/impurity-phase formation. Finally, integration into a UV-pumped phosphor-converted LED delivers spectrally stable, wide-coverage NIR illumination, highlighting configurational-entropy engineering as a practical strategy to couple functional richness with operational stability in halide-perovskite photonics.

Introduction

High-entropy materials, commonly defined as solids incorporating five or more elements in near-equatomic ratios, offer a powerful thermodynamic lever to stabilize

otherwise metastable lattices by increasing the entropic contribution ($-T\Delta S_{\text{config}}$) to the Gibbs free energy.¹⁻² This principle has reshaped materials design across alloys and ceramics and has recently entered the field of halide perovskites—an optoelectronic materials family whose operational durability is frequently limited by structural softness, interfacial reactivity, and fast ionic motion. Building on pioneering demonstrations of entropy-stabilized halide perovskite single crystals enabled by mild chemistry (e.g., Yang and co-workers)³ and subsequent extensions to diverse high-entropy perovskite compositions,⁴⁻⁶ the compositional space has expanded rapidly. Nevertheless, progress remains largely empirical: enhanced phase persistence is often observed, yet how to translate compositional complexity into device-relevant photonic functions remains insufficiently explored.⁷⁻¹¹

A key gap concerns the functional consequences and opportunities of entropy-induced disorder. For photonic solids, compositional complexity is intrinsically ambivalent. Local distortion and broadened microenvironments can suppress catastrophic phase separation, yet the same disorder can introduce nonradiative channels, amplify inhomogeneous fields, and destabilize the kinetic balance required for predictable optical operation.^{6, 12} As a result, many high-entropy perovskite emitters remain confined to conventional, single-mode luminescence, and it is still unclear whether entropy engineering can be leveraged to unlock functionally expanded optical behaviors that are inherently relevant to devices. More fundamentally, can compositional complexity be harnessed as a positive design space, where distinct element-specific roles such as sensitization and emission are functionally integrated within one lattice rather than being averaged out by disorder, thereby enabling reliable optical responses with high spectral fidelity and operational robustness?

This question is particularly timely in the context of ultrabroadband near-infrared (NIR) photonics. Wide-coverage NIR emitters are highly desirable for spectroscopy, imaging, and sensing because they can provide a single-source illumination that spans multiple absorption windows of functional groups and biological tissues.¹³⁻¹⁵ However, achieving broadband emission with high spectral fidelity under realistic conditions

remains challenging: the same environmental and kinetic factors that limit perovskite durability—moisture/oxygen attack,¹⁶⁻¹⁷ defect growth,¹⁸⁻¹⁹ and ion-migration–assisted phase evolution—also drive intensity drift and spectral instability during operation,²⁰⁻²¹ undermining quantitative readouts. High-entropy design is conceptually well aligned with this challenge. If multiple functional ions can be homogeneously integrated into one entropy-stabilized lattice, compositional complexity can, in principle, be converted into a “functional division of labor,” where a sensitizer provides a unified excitation entry and spectrally orthogonal emitters contribute separated bands across a broad spectral window—while the entropy-stabilized host helps preserve phase integrity and suppresses degradation-induced spectral drift. Such a combination would be particularly attractive for practical broadband light sources that require both functional richness and operational robustness.^{10-11, 22}

Here we establish entropy-engineered rare-earth halide double perovskite single crystals, $\text{Cs}_2\text{Na}(\text{Sb},\text{Re})\text{Cl}_6$ ($\text{Re}^{3+} = \text{Er}^{3+}, \text{Yb}^{3+}, \text{Tm}^{3+}$), as a model platform that simultaneously demonstrates functional expansion and enhanced environmental robustness. Near-equatomic B(III)-site alloying yields a single-phase high-entropy solid solution ($\Delta S_{\text{config}} \approx 1.6R$). Sb^{3+} acts as a broadband sensitizer that unifies excitation and cooperatively activates multiple lanthanide channels, converting the parent single-peak emission into a wide-coverage NIR output spanning ~ 850 – 1600 nm with three fingerprint bands at 996, 1220, and 1540 nm. This tri-peak, self-referenced signature enables redundancy-based ratiometric analysis that is intrinsically less sensitive to intensity drift, improving the reliability of solvent identification and quantitative mixture sensing. In parallel, accelerated aging tests reveal markedly enhanced tolerance to humidity and oxygen compared with single-component analogues. This improvement can be attributed to strengthened metal–halide bonding from octahedral contraction and entropy-induced lattice distortion that hinders long-range halide migration, together raising the kinetic barriers for moisture/oxygen attack and suppressing defect/impurity-phase formation. Finally, integration into a UV-pumped phosphor-converted LED yields spectrally stable, wide-coverage NIR

illumination, underscoring configurational-entropy engineering as a practical route to expand photonic functionality while strengthening operational stability.

Results and Discussion

Synthesis and Structural Characterizations of Pristine and high-entropy RHDPs

Here, high-quality pure $\text{Cs}_2\text{NaReCl}_6$, as well as $\text{Cs}_2\text{Na}(\text{Sb}_{0.2}\text{Sc}_{0.2}\text{Er}_{0.2}\text{Yb}_{0.2}\text{Tm}_{0.2})\text{Cl}_6$ (abbreviated as HEA-Yb-Tm-Er), were synthesized using an adapted hydrothermal method.²³ Typically, powder reagents including cesium chloride, sodium chloride, and rare earth hydrated chlorides were loaded into a 20-mL Teflon vessel, followed by the addition of concentrated hydrochloride (See the experimental part for details). Crystallization proceeds under a precisely controlled thermal profile (180 ± 0.5 °C for 30 h) followed by slow gradient cooling (5 °C h⁻¹). In the hydrothermal growth of rare earth-based HEHP, the slow programmed cooling stage (e.g., 5 °C/h) plays an independent and critical role. Its essence lies in the continuous and precise control of the system's supersaturation, keeping it within the kinetic metastability window, thereby suppressing explosive nucleation and driving the oriented growth of a limited number of crystal nuclei. This step is essential for high-entropy growth: slow cooling provides time for multication diffusion/equilibration, enabling homogeneous incorporation and B-site ordering in the double-perovskite lattice, while Ostwald ripening heals defects. It also drives the system toward the thermodynamic ground state, suppressing metastable or secondary phases. Consequently, programmed cooling governs crystal size, compositional uniformity, structural integrity, and phase purity.

We design HEHPs starting from the representative $\text{Cs}_2\text{NaReCl}_6$ by introducing Sb^{3+} , Sc^{3+} , Er^{3+} , Yb^{3+} and Tm^{3+} into the B(III) sites. To verify the success of synthesis, we first examined the phase purity and average crystal structure. The HEA-Yb-Tm-Er single crystals crystallize in a cubic system with the *Fm-3m* space group, exhibiting high symmetry (Figure 1a). The lattice consists of corner-sharing $[\text{NaCl}_6]^{5-}$, $[\text{SbCl}_6]^{3-}$ and $[\text{ReCl}_6]^{3-}$ octahedra, with Cs^+ cations occupying the cavities formed by these

octahedral units. The powder X-ray diffraction (PXRD) patterns of the as-prepared samples (Figure 1b) confirm the RHDP structure, as evidenced by the close match with the standard $\text{Cs}_2\text{NaTmCl}_6$ reference pattern (ICSD No. 138727). Because Er^{3+} (Yb^{3+} , Sc^{3+}) has a larger (smaller) ionic radius than Tm^{3+} , the diffraction peaks of $\text{Cs}_2\text{NaErCl}_6$ ($\text{Cs}_2\text{NaYbCl}_6$, $\text{Cs}_2\text{NaScCl}_6$) shift to lower (higher) angles in the enlarged 2θ range of 23–25°, consistent with lattice expansion and contraction. Upon multication substitution at the B(III) site, HEA-Yb-Tm-Er shows a slight peak shift, which can be attributed to the different ionic radii of Sb^{3+} (0.76 Å), Sc^{3+} (0.74 Å), Tm^{3+} (0.88 Å), Yb^{3+} (0.87 Å) and Er^{3+} (0.89 Å).²⁴ This behavior indicates a single-phase composition at the macroscopic scale.

To further clarify the structure, Rietveld refinements were carried out on the XRD data of both $\text{Cs}_2\text{NaReCl}_6$ and HEA-Yb-Tm-Er single crystals (Figure S1, Figure 1c, and Table S1). All refinements yield reliable goodness-of-fit factors ($\chi^2 < 1.5$, Rp and $\text{Rwp} < 10\%$), confirming the robustness of the models. The variations in unit-cell parameters (a, b, c) and volume (V) for $\text{Cs}_2\text{NaReCl}_6$ and HEA-Yb-Tm-Er correlate well with the corresponding XRD peak shifts (Figure 1d). These results are consistent with a homogeneous single-phase solid solution in which all cations are randomly distributed over equivalent lattice sites. The single-crystal nature and lattice periodicity of HEA-Yb-Tm-Er were then verified at the microscopic level. The selected-area electron diffraction (SAED) pattern shows sharp diffraction spots (Figure 1e left), indicating good crystallinity. High-resolution transmission electron microscopy (HRTEM) images reveal clear lattice fringes with a spacing of 0.33 nm, corresponding to the (220) plane. This spacing is smaller than that of $\text{Cs}_2\text{NaErCl}_6$, confirming lattice contraction induced by Sb^{3+} and Re^{3+} alloying (Figure 1e right).

We next evaluated the multicomponent stoichiometry and its spatial uniformity. Scanning electron microscopy (SEM) and energy-dispersive spectrometer (EDS) elemental mapping (Figure S2–S5 and Figure 1f) show that Cs, Na, Sb, Cl, Sc, Yb, Tm and Er are homogeneously distributed throughout individual HEA-Yb-Tm-Er crystals,

without detectable phase segregation. Quantitative EDS analysis gives an atomic ratio of Cs/Na/Sb/Sc/Tm/Yb/Er/Cl = 1.98/0.97/0.23/0.18/0.21/0.20/0.19/6.03, which agrees well with the ICP-OES result for HEA-Yb-Tm-Er single crystals (Figure S6, Table S2). These data confirm that the intended multicomponent composition is realized and that single-phase HEA-Yb-Tm-Er crystals are obtained. For clarity, the feeding ratios are used throughout the discussion. In addition, EDS spectra for $\text{Cs}_2\text{NaReCl}_6$ ($\text{Re}^{3+} = \text{Sc}^{3+}$, Tm^{3+} , Er^{3+} , Yb^{3+}) confirm the expected 2:1:1:6 atomic ratio for Cs:Na:Re:Cl (Figure S7), demonstrating the successful synthesis of $\text{Cs}_2\text{NaReCl}_6$.

The chemical states of the cations were further probed by X-ray photoelectron spectroscopy (XPS). Comparative XPS measurements (Figure 1g–1h and Figure S8) show that Sb and all Re ions are present in the +3 oxidation state. The full survey spectrum contains clear signals from Cs 3d, Na 1s, Sb 3d, Sc 2p, Yb 4d, Tm 4d, Er 4d and Cl 2p. As shown in Figure 1g–1i, the Sb 3d_{3/2} and 3d_{5/2} peaks appear at 539.9 and 529.5 eV, while the peak at 184.5 eV and 186.1 eV is assigned to the Yb 4d_{5/2} level and its satellite peak.^{25–27} The peaks at 169.6 and 168.0 eV correspond to the Er 4d_{3/2} and 4d_{5/2} levels, respectively, those at 177.2 and 178.6 eV are assigned to the Tm 4d_{5/2} level along with its satellite.^{28–30} Relative to the pure $\text{Cs}_2\text{NaReCl}_6$ single crystals, these binding energies exhibit systematic shifts, indicating modified local electron densities in the multicomponent lattice, consistent with an electronic-scale “cocktail effect”. Finally, the high-entropy nature was quantified by configurational entropy. A randomly mixed solid solution of HEA-Yb-Tm-Er will have a high atomic configurational entropy (ΔS_{config}), given for ideal solutions by^{31–32}

$$\Delta S_{\text{config}} = -R \left(\sum_{i=1}^N x_i \ln x_i + \sum_{j=1}^P y_j \ln y_j \right) \quad (1)$$

where N and P are the numbers of distinct ion types occupying the Na and B(III) sites, respectively, and x_i and y_j are the mole fractions of the i^{th} and j^{th} ions, respectively. High-entropy materials are defined by a configurational entropy greater than 1.5R. Accordingly, HEA-Yb-Tm-Er single crystals ($\Delta S_{\text{config}} = 1.6R$) exhibits a characteristic high-entropy nature.

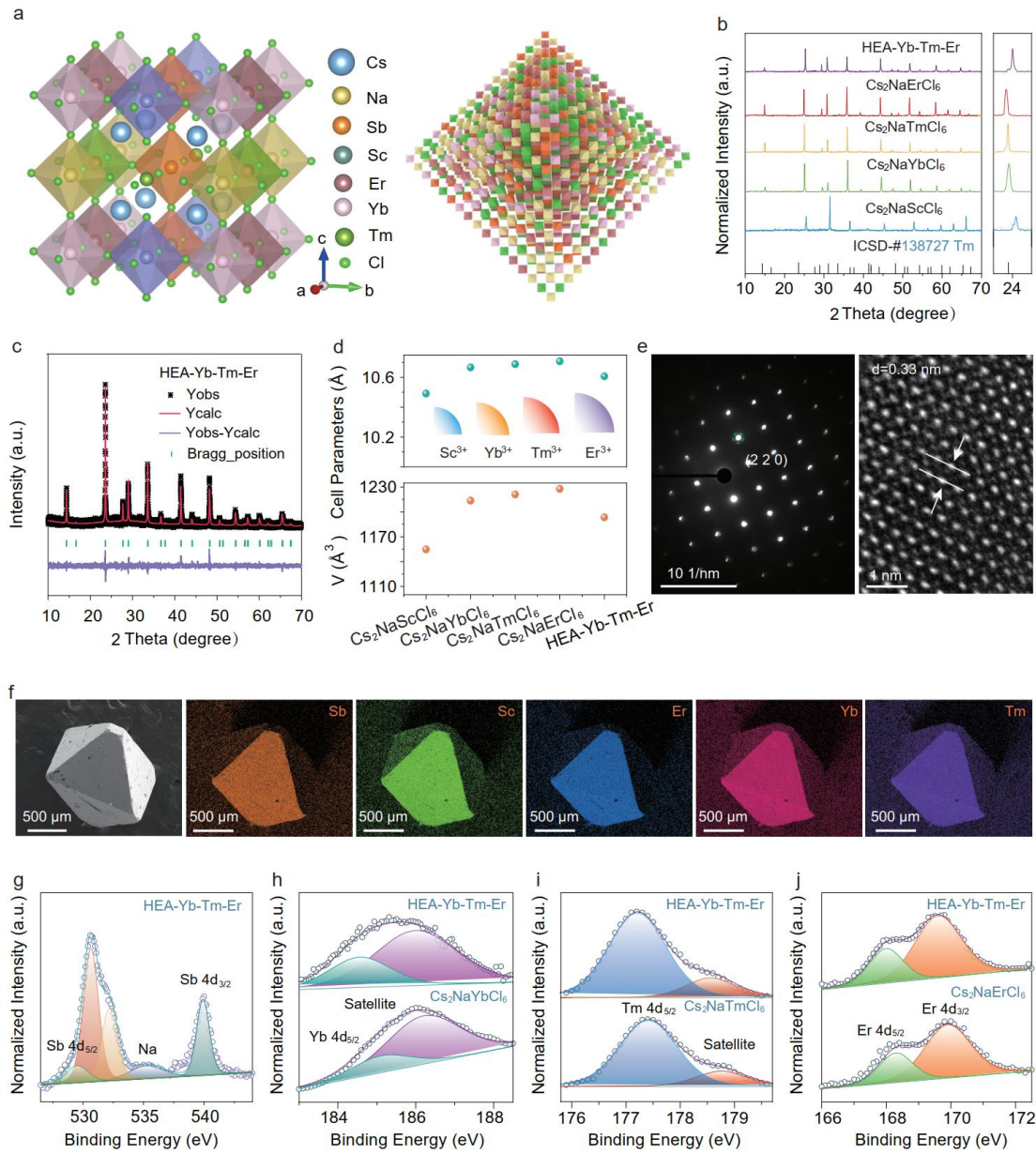


Figure 1. Structural and compositional characterization of HEA-Cs₂Na(Sb, Sc, Yb, Tm, Er)Cl₆ single crystals. a) Schematic of high-entropy double perovskite structure with five randomly distributed Sb³⁺ and Re³⁺ cations (Sc³⁺, Yb³⁺, Tm³⁺, Er³⁺). b) PXRD patterns of HEA-Yb-Tm-Er and parent Cs₂NaReCl₆ (Re³⁺ = Sc³⁺, Tm³⁺, Er³⁺, Yb³⁺) single crystals confirm single-phase structure. c) Rietveld refinement of HEA ($\chi^2 = 1.16$, Rwp = 6.3%) based on *Fm-3m* model confirms structural consistency with double perovskite lattice. d) Lattice parameters of parent crystals follow a monotonic trend with ionic radius; HEA-Yb-Tm-Er lies near the average, indicating effective multicomponent incorporation. e) SAED and HRTEM of HEA-Yb-Tm-Er show clear

lattice fringes with 0.33 nm d-spacing, corresponding to (220) planes. f) SEM and EDS mapping show uniform spatial distribution of all elements. High-resolution XPS spectra of g) Sb 3d, h) Yb 4d, i) Tm 4d and j) Er 4d orbitals in $\text{Cs}_2\text{NaReCl}_6$ and HEA-Yb-Tm-Er single crystals.

Optical Properties of $\text{Cs}_2\text{NaReCl}_6$ and HEA-Yb-Tm-Er Single Crystals

To investigate the role of each component in the high-entropy RHDPs in constructing broadband NIR emission, we conducted optical performance characterization. The absorption spectra for these materials are shown in Figure 2a. Given the focus of this study on NIR luminescence, $\text{Cs}_2\text{NaScCl}_6$ single crystals (which lack such emission) are not discussed in detail. The photoluminescence excitation (PLE) and Photoluminescence (PL) emission spectra in the visible (Vis) region (Figure S9) are provided, displaying the widely reported blue STE emission upon 250 nm excitation.³³ The $\text{Cs}_2\text{NaReCl}_6$ single crystals ($\text{Re}^{3+} = \text{Tm}^{3+}$, Er^{3+} and Yb^{3+}) exhibit distinct absorption features attributed to their respective Re^{3+} ions. In $\text{Cs}_2\text{NaTmCl}_6$ single crystals, the absorption bands at 471, 691 and 800 nm were assigned to the $^1\text{G}_4 \rightarrow ^3\text{H}_6$, $^3\text{F}_{2,3} \rightarrow ^3\text{H}_6$ and $^3\text{H}_4 \rightarrow ^3\text{H}_6$ transitions of Tm^{3+} ions, respectively.³⁴ Similarly, $\text{Cs}_2\text{NaErCl}_6$ single crystals showed absorption bands at 380 nm, 521 nm and 583 nm, corresponding to the Er^{3+} transitions $^4\text{G}_{11/2} \rightarrow ^4\text{I}_{15/2}$, $^2\text{H}_{9/2} \rightarrow ^4\text{I}_{15/2}$ and $^4\text{S}_{3/2} \rightarrow ^4\text{I}_{15/2}$, respectively.³⁵ The $\text{Cs}_2\text{NaYbCl}_6$ single crystals exhibit absorption bands at 271, 405 and 980 nm, which is attributed to the transitions of ground state (GS) $\rightarrow \text{Cl}^-$ - Yb^{3+} charge transfer band (CTB), $^2\text{F}_{5/2} \rightarrow \text{CTB}$, and $^2\text{F}_{7/2} \rightarrow ^2\text{F}_{5/2}$, respectively.³⁶ Furthermore, alongside the characteristic absorption bands of Tm^{3+} , Er^{3+} and Yb^{3+} ions, the HEA-Yb-Tm-Er single crystals demonstrate the pronounced absorption bands centered at 268 nm, 282 nm and 300-380 nm, corresponding to the $^1\text{S}_0 \rightarrow ^{1,2,3}\text{P}_1$ transition of Sb^{3+} ions, respectively.³⁷⁻³⁸ As shown in Figure 2b, $\text{Cs}_2\text{NaReCl}_6$ single crystals demonstrated the single characteristic NIR emissions at 996 nm (Yb^{3+} : $^2\text{F}_{5/2} \rightarrow ^2\text{F}_{7/2}$), 1220 nm (Tm^{3+} : $^3\text{H}_5 \rightarrow ^3\text{H}_6$) and 1540 nm (Er^{3+} : $^4\text{I}_{13/2} \rightarrow ^4\text{I}_{15/2}$), respectively. Intriguingly, HEA-Yb-Tm-Er single crystals exhibit an ultra-broadband NIR emission from 850 to 1600 nm,

integrating the transitions of Tm^{3+} , Er^{3+} and Yb^{3+} ions.

The PLE spectra elucidate the detailed origins of this emission profile. When the emission wavelengths are centered at 996, 1220, 1540 nm and ${}^3\text{P}_1-{}^1\text{S}_0$ emission of Sb^{3+} , all the PLE spectrum reveals the distinct excitation bands at 340 nm (Figure S10). These results indicate that the NIR emissions derived from energy transfer from the Sb^{3+} to Re^{3+} ions.³⁹ The normalized PLE spectra of $\text{Cs}_2\text{NaReCl}_6$ and HEA-Yb-Tm-Er single crystals, monitored at their respective NIR emissions, are shown in Figure 2c. The spectra revealed a distinct shift in dominant excitation peaks from Re^{3+} -associated bands to Sb^{3+} -related features. This spectral evolution indicates a modified excitation pathway, in which the incorporated Sb^{3+} ions act as critical sensitizers.⁴⁰ By providing a broad absorption band around 340 nm, they enable efficient energy transfer to Re^{3+} ions upon single-wavelength excitation, thereby maximizing the overall luminescence output. Despite the prevalence of nonradiative cross-relaxation in multi-dopant systems, the incorporation of multiple Re^{3+} ions here show no apparent luminescence quenching (Figure S11). This is attributed to the key advantage provided by the large unit cell of $\text{Cs}_2\text{NaReCl}_6$: it increases the average inter-Re distance (to ~ 7.6 Å), more than twice that in NaYF_4 (~ 3.5 Å)—the $1/d^6$ dependence of energy transfer reduces long-range migration to quenching centers.⁴¹⁻⁴² This expanded separation effectively suppresses energy migration among Re^{3+} ions, thereby enabling the precise tuning of diverse emission profiles, ranging from 4f–4f transitions to broadband STE emission.

The time-resolved decay curves of $\text{Cs}_2\text{NaReCl}_6$ and HEA-Yb-Tm-Er single crystals have been measured to study the radiative processes. All the samples exhibited the biexponential fitting decay with nonradiative (τ_1) and radiative recombination (τ_2). Compared with $\text{Cs}_2\text{NaReCl}_6$ single crystals, the HEA-Yb-Tm-Er single crystals exhibited the attenuated nonradiative and the promoted radiative recombination, as evidenced by their PL lifetimes (Figure 2d, Table S3). This behavior may be caused by higher transport energy barriers due to the lattice distortion in high-entropy materials.⁴³ It reduces their diffusion and nonradiative recombination probability, thereby extending the lifetime. The measured Photoluminescence Quantum Yield (PLQY) are 19.9%, 24.9%

and 25.1% for $\text{Cs}_2\text{NaErCl}_6$, $\text{Cs}_2\text{NaTmCl}_6$ and $\text{Cs}_2\text{NaYbCl}_6$ single crystals, respectively (Figure 2e). While Sb^{3+} is known to sensitize emission via its broad $^3\text{P}_1$ state, the PLQY of HEA-Yb-Tm-Er single crystals are limited to ~22.0 %. This lower efficiency is attributed to the lattice strain and structural defects arising from the incorporation of multiple Re^{3+} ions, which promote non-radiative decay and thus reduce the overall PLQY.

To further verify the spectral tunability of NIR emissions in the high-entropy system, we synthesized single-luminescent-center $\text{Cs}_2\text{Na}(\text{Sb}_{0.2}\text{Sc}_{0.2}\text{Y}_{0.2}\text{Gd}_{0.2}\text{Tm}_{0.2})\text{Cl}_6$ (HEA-Tm), $\text{Cs}_2\text{Na}(\text{Sb}_{0.2}\text{Sc}_{0.2}\text{Y}_{0.2}\text{Gd}_{0.2}\text{Er}_{0.2})\text{Cl}_6$ (HEA-Er), and $\text{Cs}_2\text{Na}(\text{Sb}_{0.2}\text{Sc}_{0.2}\text{Y}_{0.2}\text{Gd}_{0.2}\text{Yb}_{0.2})\text{Cl}_6$ (HEA-Yb) single crystals and investigated their NIR emission characteristics. The structural characterizations and optical properties are presented in Figures S12-S13. Under 340 nm excitation, HEA-Tm, HEA-Er, and HEA-Yb single crystals exhibited characteristic NIR emissions identical to those of $\text{Cs}_2\text{NaReCl}_6$ (Figure S14-S16). In contrast, the strategy of multi-emissive-center high-entropy systems represents a paradigm shift. Its value stems from the fundamental combination of entropy-stabilized phases and cooperative elemental effects, which in our system collectively unlock superior and readily tunable broadband emission alongside designer functionalities. The NIR emission lifetimes in HEA-Tm, HEA-Er, and HEA-Yb single crystals followed the same trend as those in HEA-Yb-Tm-Er single crystals (Figure S17), with detailed fitting parameters summarized in Table S3.

Furthermore, we conducted first-principles calculations on $\text{Cs}_2\text{NaSbCl}_6$, $\text{Cs}_2\text{NaReCl}_6$ ($\text{Re}^{3+} = \text{Sc}^{3+}, \text{Tm}^{3+}, \text{Er}^{3+}, \text{Yb}^{3+}$) and HEA-Yb-Tm-Er single crystals to investigate the potential impact of Sb^{3+} and Re^{3+} ions alloying in multicomponent HEA-Yb-Tm-Er single crystals on their electronic band structures and optical properties.⁴⁰ We first investigated the electronic structure using multiple computational methods to estimate the band gap. Although the PBE method is known to be unreliable for predicting energy gaps, the HSE functional generally provides a good estimation. To ensure both the comparability and the accuracy of our electronic structure analysis, we adopted a tiered computational approach. Initial calculations were performed using the Perdew-Burke-Ernzerhof (PBE) functional to establish a baseline compatible with the

extensive body of literature that employs this method. As anticipated and illustrated in Figure S18, the PBE functional significantly underestimates the band gap.⁴⁴ Nevertheless, this step provided critical validation of our structural models against prior reported results.⁴⁵⁻⁴⁷ Subsequently, the more accurate Heyd-Scuseria-Ernzerhof (HSE06) hybrid functional was employed.

Parent $\text{Cs}_2\text{NaSbCl}_6$ and $\text{Cs}_2\text{NaReCl}_6$ ($\text{Re}^{3+} = \text{Sc}^{3+}, \text{Tm}^{3+}, \text{Er}^{3+}, \text{Yb}^{3+}$) display the band gap of 3.89, 5.56, 6.77, 6.72 and 6.76 eV, respectively (Figure S19 left). The projected density of states (PDOS) analysis indicates that the valence band maximum (VBM) is dominated by Cl 3p orbitals, while the conduction band minimum (CBM) comprises a mixture of Sb 5p, Sc 3d, Tm 4d, Er 4d, and Yb 4d orbitals, along with Cl 3p states (Figure S19 right). To elucidate the sensitization role of Sb in the multicomponent HEA-Yb-Tm-Er, we also computed the PDOS of the $\text{Cs}_2\text{Na}(\text{Sc}_{0.25}\text{Yb}_{0.25}\text{Tm}_{0.25}\text{Er}_{0.25})\text{Cl}_6$. Comparative PDOS analysis reveals that Sb^{3+} doping creates a new sensitization center by introducing Sb 5s states above the VBM and Sb 5p states below the CBM. The feasible 5s–5p optical transitions of this center enable efficient energy transfer within the HEA-Yb-Tm-Er single crystals. Guided by above experimental and first principles calculations results, the mechanism is proposed that incorporation of Sb^{3+} ion unifies the absorption channel, establishing an efficient photoexcitation-recombination in HEA-Yb-Tm-Er single crystals (Figure 2h). Upon excitation at 340 nm, the Sb^{3+} ion was excited from the ${}^1\text{S}_0$ to the ${}^3\text{P}_1$ state, which then underwent dynamic Jahn–Teller distortion, resulting in broad blue emission centered at 460 nm via the ${}^3\text{P}_1 \rightarrow {}^1\text{S}_0$ transition. Simultaneously, part of the STE energy was non-radiatively transferred to nearby Yb^{3+} , Tm^{3+} and Er^{3+} ions, giving rise to intense NIR emissions at 996, 1220 and 1540 nm. This process collectively achieves a broadband NIR emission spanning approximately 850-1600 nm.

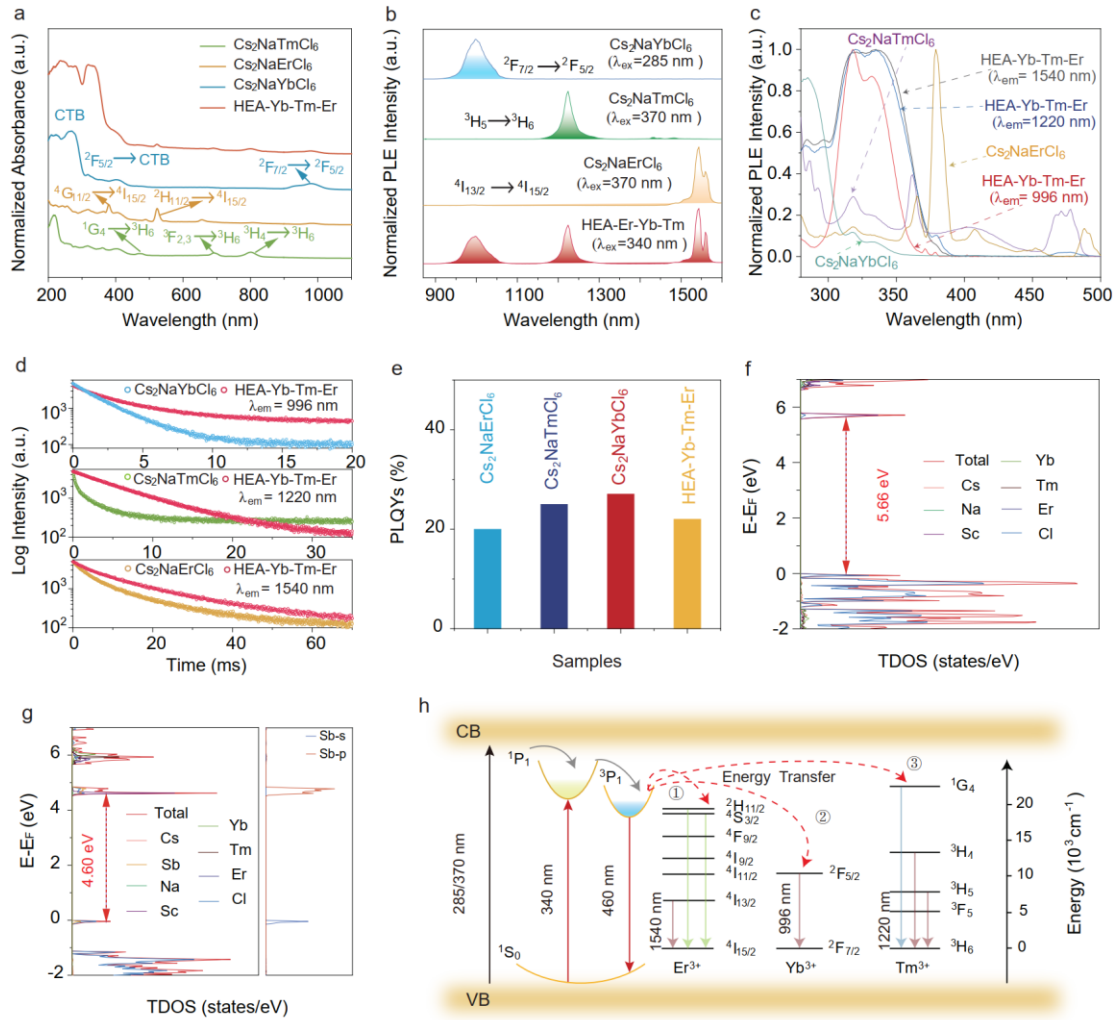


Figure 2. Optical properties of $\text{Cs}_2\text{NaReCl}_6$ and HEA-Yb-Tm-Er single crystals.

a) UV-vis-NIR absorption spectra of $\text{Cs}_2\text{NaReCl}_6$ (Re³⁺ = Er³⁺, Yb³⁺, Tm³⁺) and HEA-Yb-Tm-Er single crystals. b) NIR PL spectra of $\text{Cs}_2\text{NaYbCl}_6$, $\text{Cs}_2\text{NaTmCl}_6$, $\text{Cs}_2\text{NaErCl}_6$, and HEA-Yb-Tm-Er. c) Normalized PLE spectra monitored at different emission wavelengths (996, 1220, and 1540 nm), illustrating excitation pathways for individual Re³⁺ centers in both parent and HEA crystals. d) Time-resolved PL decay curves of $\text{Cs}_2\text{NaReCl}_6$ and HEA-Yb-Tm-Er single crystals, recorded at emission wavelengths of 996 nm (Yb³⁺), 1220 nm (Tm³⁺), and 1540 nm (Er³⁺). e) Absolute PLQYs of $\text{Cs}_2\text{NaReCl}_6$ and HEA-Yb-Tm-Er single crystals under UV excitation. f) PDOS for $\text{Cs}_2\text{Na}(\text{Sc}_{0.25}\text{Yb}_{0.25}\text{Tm}_{0.25}\text{Er}_{0.25})\text{Cl}_6$. g) PDOS for HEA-Yb-Tm-Er. h) Schematic illustration of the PL processes and energy-transfer pathways among Er³⁺, Yb³⁺, and Tm³⁺ ions in HEA-Yb-Tm-Er single crystals.

Environmental Stability Assessment of $\text{Cs}_2\text{NaReCl}_6$ and HEA-Er-Yb-Tm single

crystals

Given the well-documented environmental sensitivity of perovskite materials, we systematically evaluated $\text{Cs}_2\text{NaReCl}_6$ ($\text{Re}^{3+} = \text{Sc}^{3+}, \text{Tm}^{3+}, \text{Er}^{3+}, \text{Yb}^{3+}$) and HEA-Yb-Tm-Er single crystals under harsh conditions of prolonged high-humidity and oxygen exposure, with the dual aims of assessing their robustness and elucidating the role of the high-entropy effect. As moisture represents a critical environmental stressor, we first examined the behavior under controlled humidity. All samples were subjected to accelerated aging tests under controlled high-humidity conditions (100% RH) at ambient temperature (25-30°C), with periodic XRD characterization to analyze the structural evolution. After being subjected to a 12-hour exposure, $\text{Cs}_2\text{NaTmCl}_6$ exhibited additional diffraction peaks corresponding to NaCl and TmCl_3 in its XRD pattern (Figure 3a), suggesting the onset of partial decomposition. With prolonged exposure time, the XRD peaks of NaCl and TmCl_3 intensified while the crystalline peaks of $\text{Cs}_2\text{NaTmCl}_6$ gradually weakened. After 24 hours under high relative humidity (100% RH), the diffraction intensities of impurity phases became comparable to those of $\text{Cs}_2\text{NaTmCl}_6$, indicating near-complete sample decomposition. Similar degradation behavior was observed for other $\text{Cs}_2\text{NaReCl}_6$ ($\text{Re}^{3+} = \text{Sc}^{3+}, \text{Er}^{3+}, \text{and Yb}^{3+}$) single crystals under identical conditions, with extensive decomposition occurring within 24 hours (Figure S20). The high ionic mobility within perovskite lattices, particularly for halide ions, is a major driver of structural degradation. Migrating ions accumulate at interfaces and grain boundaries, nucleating secondary phases and creating non-radiative recombination centers that severely compromise optical performance.⁴⁸

In contrast, the HEA-Yb-Tm-Er single crystals demonstrated significantly enhanced phase stability under high-humidity conditions, as their XRD patterns showed only minimal NaCl impurity formation after 24-hour exposure under identical conditions (Figure 3b). Furthermore, the moisture absorption characteristics of both $\text{Cs}_2\text{NaReCl}_6$ ($\text{Re}^{3+} = \text{Tm}^{3+}, \text{Er}^{3+}, \text{Yb}^{3+}$) and HEA-Yb-Tm-Er single crystals were quantitatively compared using gravimetric analysis. The results demonstrated that the HEA-Yb-Tm-Er single crystals exhibited significantly lower water adsorption capacity

than their single-component counterparts, demonstrating enhanced moisture resistance (Figure 3c). The enhancement in humidity stability can be attributed to two primary factors: (1) Bonding enhancement and kinetic hindrance. Compared to the pure $\text{Cs}_2\text{NaReCl}_6$ single crystals, the average contraction of the $[\text{B}\text{Cl}_6]^{3-}$ octahedra ($\text{B}^{3+} = \text{Sb}^{3+}, \text{Sc}^{3+}, \text{Yb}^{3+}, \text{Tm}^{3+}$ and Er^{3+}) in HEA-Yb-Tm-Er single crystals shortens the B–Cl bond distance. This promotes greater orbital overlap and an increased covalent contribution to the bonding, resulting in a higher bond dissociation energy and more localized electron density along the bond axis. Consequently, the activation energy required for water molecules to coordinate to the B^{3+} center and cleave the B–Cl bonds during hydrolysis is substantially raised. This elevated kinetic barrier effectively retards the moisture-driven degradation pathway, leading to significantly improved humidity stability. (2) High-Entropy lattice distortion. The incorporation of multiple Sb^{3+} and Ln^{3+} ions with mismatched ionic radii induces severe lattice distortion. This pronounced distortion creates a complex, high-energy local environment that acts as an effective kinetic barrier, impeding the long-range migration of Cl^- ions within the perovskite lattice.

The optical microscopy images in Figure 3d and Figure S21 document the hygroscopic degradation process of $\text{Cs}_2\text{NaReCl}_6$ ($\text{Re}^{3+} = \text{Sc}^{3+}, \text{Tm}^{3+}, \text{Er}^{3+}, \text{Yb}^{3+}$) and HEA-Yb-Tm-Er single crystals under high-humidity conditions over 0-24 hours. The degradation of the $\text{Cs}_2\text{NaReCl}_6$ under high humidity follows a well-defined sequence, progressing from initial surface attack to complete structural collapse. The process begins with the adsorption and localized accumulation of H_2O at surface defects, which gradually induces micro-crack formation as hydrolysis proceeds. Over time, these cracks propagate and coalesce, causing the edges of the single crystal to become progressively blurred and irregular. Ultimately, cumulative chemical and mechanical damage leads to loss of macroscopic integrity (as evidenced by the impurity phase XRD peaks), transforming the well-defined single crystal into a fragmented state. In striking contrast, the HEA-Yb-Tm-Er single crystals maintained structural integrity throughout the 24-hour test, showing neither large amount of water adsorption nor surface morphological changes. These results indicated that the high configurational entropy

inherent to the high-entropy design thermodynamically stabilizes the single-phase solid-solution. In a humid environment, this stabilization effect enables the HEA-Yb-Tm-Er single crystals to resist the nucleation and growth of degradation-prone, moisture-sensitive impurity phases.

To further investigate whether the enhanced humidity stability is entropy-driven, we conducted comparative humidity stability tests (100% RH, 25-30°C) on HEA-Tm, HEA-Er, and HEA-Yb single crystals, respectively. The XRD characterization demonstrated that all RHDPS exhibited similar stability, showing weak NaCl impurity peaks after 24-hour exposure (Figure S22). The HEA-Tm, HEA-Er, and HEA-Yb single crystals exhibited significantly enhanced moisture resistance compared to $\text{Cs}_2\text{NaReCl}_6$ ($\text{Re}^{3+} = \text{Tm}^{3+}$, Er^{3+} , and Yb^{3+}) counterparts (Figure S23). These collective results confirm configurational entropy stabilization as the dominant mechanism underlying the exceptional environmental stability of high-entropy alloy single crystals.

The NIR PL spectra of $\text{Cs}_2\text{NaReCl}_6$ ($\text{Re}^{3+} = \text{Tm}^{3+}$, Er^{3+} , and Yb^{3+}), HEA-Re ($\text{Re}^{3+} = \text{Tm}^{3+}$, Er^{3+} , and Yb^{3+}), and HEA-Yb-Tm-Er single crystals were measured after 24-hour exposure to controlled humidity conditions (100% RH, 25°C). It can be observed that the NIR PL intensity of $\text{Cs}_2\text{NaTmCl}_6$ single crystals exhibited a progressive decrease during humidity exposure, remaining only ~2 % of its initial PL intensity after 24 hours (Figure 3e top and Figure 3f). Similarly, the NIR PL emissions of both $\text{Cs}_2\text{NaYbCl}_6$ and $\text{Cs}_2\text{NaErCl}_6$ single crystals showed complete quenching after 24-hour exposure under identical high-humidity conditions (100% RH, 25°C) (Figure S24 and Figure 3f). The structural degradation directly correlates with a significant deterioration in optical performance. Notably, HEA-Er-Yb-Tm and HEA-Re ($\text{Re}^{3+} = \text{Tm}^{3+}$, Er^{3+} , and Yb^{3+}) single crystals retained 80%, 34%, 21%, and 15% of their initial NIR PL intensities after 24-hour humidity exposure, respectively (Figures 3e bottom, 3f, and S25). Combined structural characterization and PL studies confirm that entropy stabilization effects significantly improve the humidity resistance of RHDPS materials.

The potential application of HEA-Yb-Tm-Er single crystals in ambient NIR photonics necessitates a fundamental understanding of its degradation pathways in air.

Beyond single-factor tests, the interplay between oxygen and moisture is often decisive for long-term performance. Therefore, we investigate the synergistic effects of elevated O₂ concentration (90%) and approximately 50–60% RH on the HEA-Yb-Tm-Er single crystals stability. XRD analysis (Figures 3g, S26-S27) reveals impurity phase diffraction peaks in Cs₂NaReCl₆ (Re³⁺ = Tm³⁺, Er³⁺, and Yb³⁺) single crystals, while HEA-Re (Re³⁺ = Tm³⁺, Er³⁺, and Yb³⁺) and HEA-Yb-Tm-Er systems remain phase-pure. After 24-hour exposure, the NIR PL intensities of Cs₂NaReCl₆ (Re³⁺ = Tm³⁺, Er³⁺, and Yb³⁺), HEA-Re (Re³⁺ = Tm³⁺, Er³⁺, and Yb³⁺), and HEA-Yb-Tm-Er single crystals retained 31%, 26%, 30%, 84%, 63%, 58%, and 85% of their initial values, respectively (Figures 3h-i, S28-S29). The observed crystal degradation under oxygen exposure results from Cs⁺-O₂ reactions that form charge-blocking barriers. These barriers immobilize charges at defect sites and electron traps, inhibiting radiative recombination and consequently reducing NIR PL intensity.⁴⁹ It is further confirmed by the measured results that high configurational entropy stabilizes HEA-Yb-Tm-Er single crystals against decomposition and oxygen-induced reactions. The enhanced stability under high O₂ concentration (90%) and moderate humidity (\approx 50–60% RH) can be attributed to a mechanism analogous to that observed above in HEA-Yb-Tm-Er: the severe lattice distortion creates a high energy barrier for ion migration. This effectively retards the inward diffusion of corrosive species (O²⁻ and H₂O) as well as the outward diffusion of Re³⁺ ions, thereby suppressing the overall degradation kinetics.

Further, the enhanced environmental stability of the HEA-Yb-Tm-Er single crystals was evaluated by calculating their decomposition enthalpy (ΔH) and Gibbs free energy (ΔG) as a measure of thermodynamic stability based on DFT. Figure S30 (blue line) presents the ΔH of six random configurations of HEA-Yb-Tm-Er single crystals (~320 atoms), with values ranging up to 139.2 meV/f.u.. The $T\Delta S_{\text{config}}$ for HEA-Yb-Tm-Er single crystals is -35.6 meV. Consequently, the ΔG , derived from $\Delta G = \Delta H - T\Delta S_{\text{config}}$, reaches a maximum value of 174.8 meV/f.u. (Figure S30, red line). For the pure Cs₂NaSbCl₆ and Cs₂NaReCl₆ (Re³⁺ = Sc³⁺, Tm³⁺, Yb³⁺, and Er³⁺), the ΔH are 108.1, 128.9, 141.5, 154.0, and 174.0 meV/f.u., respectively. Due to their $T\Delta S_{\text{config}}$ is 0 meV,

the corresponding ΔG are identical to the ΔH values. A comparison reveals that HEA-Yb-Tm-Er single crystals possess a larger (more positive) ΔG than pure $\text{Cs}_2\text{NaSbCl}_6$ and $\text{Cs}_2\text{NaReCl}_6$ single crystals. Consequently, the more positive ΔG of HEA-Yb-Tm-Er single crystals indicates that its decomposition is less spontaneous, which correlates with enhanced environmental stability. This work demonstrates that configurational entropy stabilizes HEA-Yb-Tm-Er single crystals achieve a critical unification of broadband, tunable NIR emission and intrinsic environmental robustness. This synergy, rooted in high-entropy-enabled lattice stabilization and enhanced metal-halide bonding, opens a new avenue for the development of stable, high-performance NIR-emitting materials with wide spectral coverage.

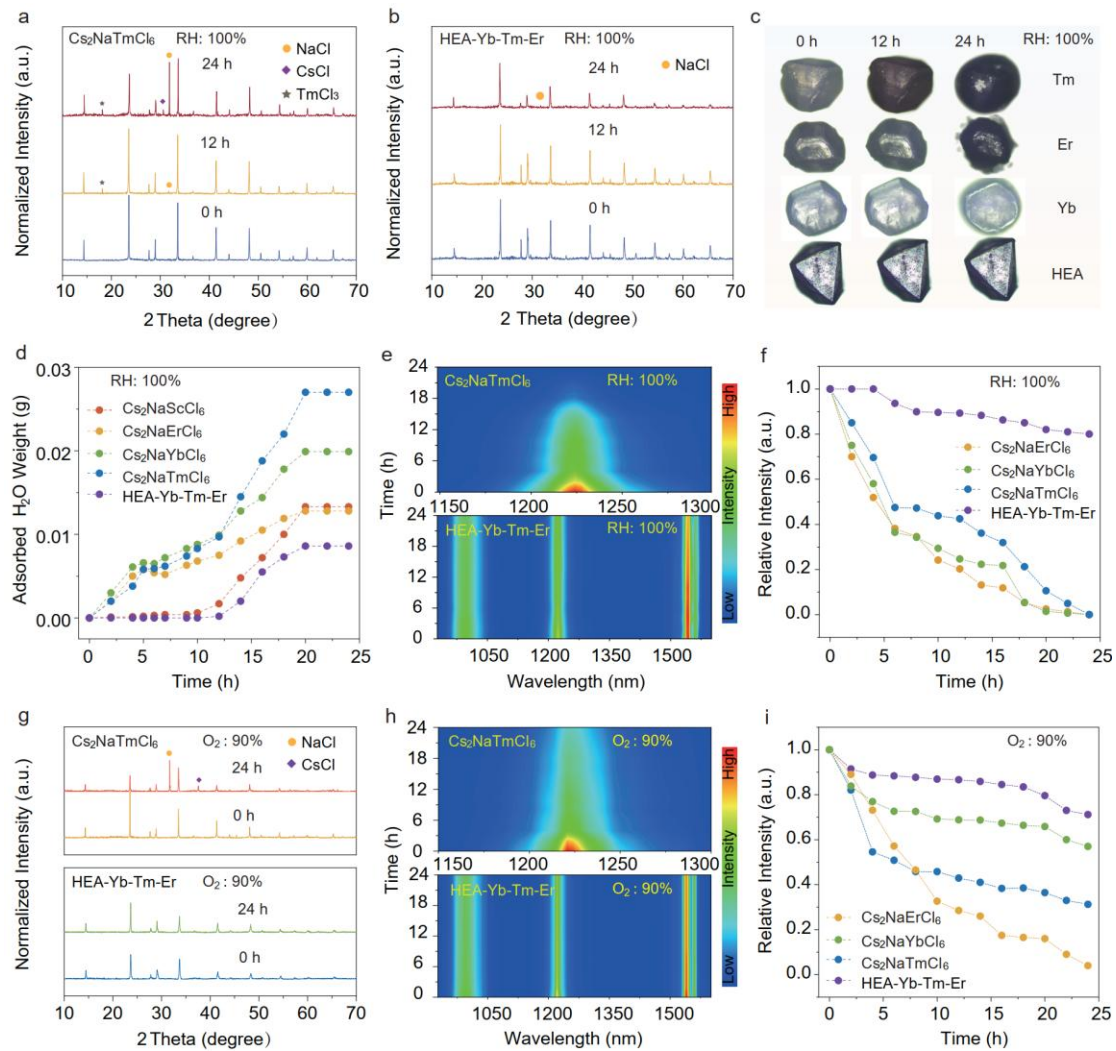


Figure 3. Structural and optical stability evaluation of $\text{Cs}_2\text{NaReCl}_6$ ($\text{Re}^{3+} = \text{Tm}^{3+}$, Er^{3+} , Yb^{3+}) and HEA-Yb-Tm-Er single crystals under humid and oxidative

conditions. XRD patterns of $\text{Cs}_2\text{NaTmCl}_6$ a) and HEA-Yb-Tm-Er b) single crystals after 0, 12, and 24 h exposure at 100% RH. c) Optical images of the crystals under 100% RH at different durations. d) Time-dependent water absorption measured by weight gain. e) Evolution of NIR PL spectra of $\text{Cs}_2\text{NaTmCl}_6$ (top) and HEA-Yb-Tm-Er (bottom) under 100% RH. f) Relative NIR PL intensity as a function of time for all samples under 100% RH. XRD g) and time-resolved NIR PL spectra h) of $\text{Cs}_2\text{NaTmCl}_6$ (top) and HEA-Er-Yb-Tm (bottom) under oxygen atmosphere (O_2 , 90%; 50–60% RH). i) Time-dependent PL degradation under O_2 for all samples.

Application of Ultrabroadband NIR Emission

HEA-Yb-Tm-Er single crystals leverage the distinct optical characteristics of multiple elements, achieving an ultrabroadband single-component NIR emission (850–1600 nm) under UV or blue light excitation. This property prompted us to construct NIR LEDs by combining these single-component, wide-coverage NIR-emitting materials with a 340 nm UV chip. Figure S31 displays the bias-dependent electroluminescence (EL) spectra of the fabricated NIR LED, which demonstrates spectral tunability over an ultrabroadband range showing distinct peaks at 996, 1220, and 1540 nm. As the drive voltage increases, only the intensity of the spectra changes, while the spectral profile remains constant, demonstrating excellent spectral stability for practical applications.

The broad application potential of NIR light sources—including in night vision, food analysis, and bioimaging—continues to motivate significant research and development efforts.⁵⁰⁻⁵¹ Figure 4a schematically illustrates the principle of NIR imaging using an LED, showing how it enables the capture of detailed images. Figure 4b–d display a comparison under natural light (top) and NIR-LED illumination (bottom), with corresponding high-contrast, black-and-white NIR camera images shown below, clearly revealing fine details through NIR imaging. When the as-prepared NIR-LED is used for imaging human tissue, the transmitted light reveals the venous blood vessels in the palm, as captured by the NIR camera (Figure 4c). This contrast is attributed to the differential absorption of specific NIR wavelengths by chromophores

in the blood.¹⁴ The capability of NIR spectroscopy for early and non-destructive detection of food spoilage underpins its practical utility. While the apples appear fresh under visible light (Figure 4d top), the NIR image under pc-LED illumination (Figure 4d bottom) shows a dark region on one, corresponding to elevated moisture content—an early spoilage indicator. This contrast is attributed to the absorption of NIR light by water hydroxyl groups, which attenuates the reflected signal and implies a reduced shelf life for that apple. The operational stability of the NIR LED was evaluated over an extended period. As shown in Figure S32, the device maintained stable emission intensity with minimal variation during 50 hours of continuous operation. Combined with its intrinsic NIR spectral features—including invisibility to the human eye and good tissue penetration—this robust performance supports its potential use in night-vision and bioimaging applications.

Capitalizing on the three fingerprint NIR-II emission peaks (996, 1220, 1540 nm) of HEA-Yb-Tm-Er single crystals across their tunable 1000–1700 nm range, a ratiometric detection strategy for organic solvents is achieved. The differential response of these peaks to characteristic absorptions of functional groups (e.g., O—H, C—H, N—H) grants this method higher selectivity and robustness against interference than single-wavelength detection, ensuring more reliable quantitative analysis and a richer understanding of solvent properties.⁵² The setup shown in Figure 4e consists of an NIR LED source, an integrating sphere, and an optical spectrometer, used to characterize samples via transmission or reflection. Following excitation by the LED, NIR-II light interacts with the sample and is directed to the spectrometer for spectral acquisition, with data subsequently stored and processed on a computer. The absorption spectra of ten solvents—including water (H₂O), methanol (MeOH), ethanol (EtOH), hexane (n-hexane), propylene glycol monomethyl ether (PG ME), acetic acid (HAc), octylamine (C₈-NH₂), aniline (Ph-NH₂), *N*, *N*-Dimethylformamide (DMF), and tetrahydrofuran (THF) -are clearly resolved (Figure S33). We performed chemometric analysis based on the initial NIR spectra of HEA-Yb-Tm-Er and the solvent-transmitted NIR spectra. The intensity and peak position variations in the NIR spectra of the ten solvents were

detected, enabling solvent discrimination. Three characteristic absorption bands are observed at 950–1000 nm, 1150–1250 nm, and 1400–1550 nm, corresponding to the overtones of O–H, N–H and C–H stretching modes, respectively (Figure 4f-g).⁵³⁻⁵⁴

Moreover, the three characteristic NIR emission peaks of HEA-Yb-Tm-Er single crystals were used to define ratiometric variables ($x = I_{1540}/I_{996}$, $y = I_{1540}/I_{1220}$, $z = I_{1220}/I_{1540}$), enabling quantitative comparison across solvents with different functional groups. As plotted in Figure 4f, these three intensity ratios map each solvent to a distinct coordinate in a three-dimensional space. In this ratiometric coordinate system, solvents are spatially separated according to their unique spectral-response patterns, which significantly enhances identification accuracy of solvents and provides a clear visual basis for discrimination. Importantly, using three independent ratiometric variables provides built-in redundancy and cross-validation, which suppresses intensity fluctuation artifacts (e.g., excitation power, optical alignment, and sample loading) and thereby improves identification accuracy. A ratiometric approach was further applied to discriminate binary solvent mixtures, using H₂O-DMF as a model system. The corresponding spectral changes are displayed in Figure 4i (top), where the intensities of the three NIR peaks (996, 1220, and 1540 nm) decrease systematically with increasing DMF content. This trend can be quantified via three intensity ratios, which all show strong linear correlations as the H₂O concentration rises from 20 vol% to 100 vol%. The obtained correlation coefficients (R^2) of 0.9964, 0.9971, and 0.9980 confirm the reliability and quantitative consistency of the ratiometric detection system (Figure 4i, bottom).

Building on the ratiometric multi-peak approach developed for mixed-solvent discrimination, we further extended its application to the quantitative assessment of freshness in solid biological samples. The NIR spectral responses clearly differentiated orange peel subjected to different drying treatments (fresh, 0.5 h at 80 °C, and 1 h at 80 °C), as shown in Figure 4j. The systematic spectral variations—such as intensity changes or peak shifts in regions associated with O–H and C–H vibrations—directly correlate with the loss of moisture and the resulting physical withering. In summary,

this study not only reports a class of high-performance and stable NIR-emitting materials, but also establishes a universal strategy for the synergistic regulation of optical properties and environmental stability via high-entropy design. It thereby lays a material foundation for next-generation advanced NIR optoelectronic devices capable of reliable operation under harsh conditions, and motivates further exploration and creation of complex functional materials across interdisciplinary fields.

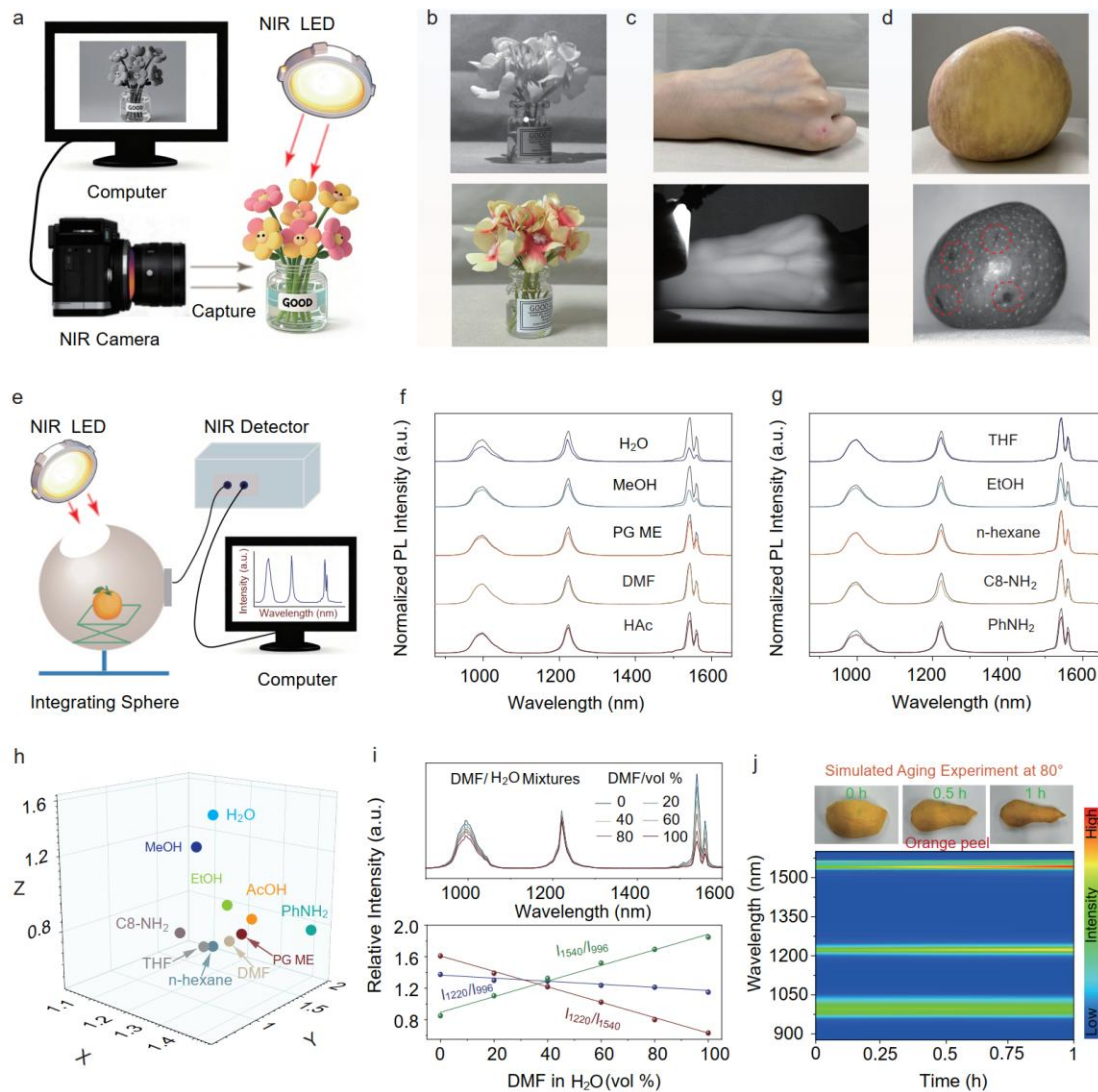


Figure 4. Tri-peak, self-referenced NIR-II photonics enabled by the HEA-Yb-Tm-Er phosphor-converted LED. a) Schematic of NIR imaging with the as-fabricated broadband NIR LED and an NIR camera. b-d) Representative imaging under ambient visible illumination (top) and NIR-LED illumination (bottom), with NIR-camera images highlighting enhanced contrast and subsurface information. e) Schematic of the

spectroscopic sensing platform (NIR LED + integrating sphere + spectrometer). f, g) Normalized transmitted spectra of ten solvents, showing solvent-specific modulation of the three fingerprint peaks. h) 3D ratiometric feature space constructed from $x = I_{1540}/I_{996}$, $y = I_{1540}/I_{1220}$, $z = I_{1220}/I_{1540}$ for solvent identification, leveraging internal normalization to suppress intensity drift and baseline/scattering variations. i) DMF/H₂O mixture quantification: spectra (top) and linear dependence of ratiometric variables on composition (bottom). j) Proof-of-concept freshness assessment: photographs (top) and time-dependent NIR spectral maps (bottom) of orange peel during thermal aging (80 °C), revealing systematic spectral evolution associated with dehydration.

Conclusion

In summary, we convert configurational-entropy-enabled compositional complexity into device-relevant ultrabroadband NIR photonics by establishing a high-entropy rare-earth halide double perovskite single-crystal platform, Cs₂Na(Sb,Sc,Er,Yb,Tm)Cl₆. Near-equiautomic B(III)-site alloying yields a single-phase cubic solid solution ($\Delta S_{\text{config}} \approx 1.6R$) with homogeneous multicomponent incorporation, allowing element-specific roles to be functionally integrated rather than averaged out. Sb³⁺ serves as a broadband sensitizer that unifies excitation and cooperatively activates Er³⁺/Yb³⁺/Tm³⁺ emission centers, transforming the parent single-mode luminescence into wide-coverage NIR output spanning ~850–1600 nm with a tri-peak fingerprint signature. This self-referenced spectral redundancy enables ratiometric analysis that is intrinsically less susceptible to intensity drift, supporting reliable solvent identification and quantitative mixture sensing. Beyond functional expansion, the high-entropy crystals exhibit markedly improved tolerance to humidity and oxygen compared with single-component Cs₂NaReCl₆ analogues, retaining NIR emission under harsh environments. This robustness is experimentally attributed to (i) octahedral contraction–strengthened metal–halide bonding that raises the kinetic barrier for moisture-triggered coordination and bond cleavage, and (ii) entropy-induced local lattice distortion that creates a rugged migration landscape and suppresses long-range halide transport, thereby inhibiting ion-migration–assisted defect/impurity–phase

formation. Finally, integration into a 340 nm-pumped phosphor-converted LED delivers spectrally stable, wide-coverage NIR illumination, highlighting configurational-entropy engineering as a practical route to simultaneously expand photonic functionality and strengthen operational stability in halide-perovskite materials.

Experimental Section

Material: Cesium chloride (CsCl, 99.99%), sodium chloride (NaCl, 99.99%), antimony chloride hexahydrate ($\text{SbCl}_3 \cdot 6\text{H}_2\text{O}$, 99.99%), erbium chloride hexahydrate ($\text{ErCl}_3 \cdot 6\text{H}_2\text{O}$, 99.99%), ytterbium chloride hexahydrate ($\text{YbCl}_3 \cdot 6\text{H}_2\text{O}$, 99.99%), thulium chloride hexahydrate ($\text{TmCl}_3 \cdot 6\text{H}_2\text{O}$, 99.99%), yttrium chloride hexahydrate ($\text{YCl}_3 \cdot 6\text{H}_2\text{O}$, 99.99%), and gadolinium chloride hexahydrate ($\text{GdCl}_3 \cdot 6\text{H}_2\text{O}$, 99.95%) were purchased from Aladdin. Scandium chloride hexahydrate ($\text{ScCl}_3 \cdot 6\text{H}_2\text{O}$, 99.99%) was purchased from Macklin Biochemical Co.,Ltd. Hydrochloric acid (HCl, 37wt% in water) were purchased from Sinopharm Chemical Reagent Co., Ltd, China. All chemicals were used directly without further purification.

Synthesis of $\text{Cs}_2\text{NaReCl}_6$ ($\text{Re}^{3+}=\text{Er}^{3+}, \text{Yb}^{3+}, \text{Tm}^{3+}, \text{Sc}^{3+}, \text{Y}^{3+}, \text{Gd}^{3+}$) single crystals

The $\text{Cs}_2\text{NaReCl}_6$ single crystals were synthesized *via* the hydrothermal method following established procedures. 2 mmol CsCl, 1 mmol NaCl, 1 mmol $\text{ReCl}_3 \cdot 6\text{H}_2\text{O}$ were dissolved in 4 mL HCl solvent (12 M) in a 20 mL Teflon-lined container. The mixture was subjected to heating at 180 °C for 12 hours using a stainless-steel Parr autoclave. And then, the reactor was cooled to the 25°C within 30 h. The resulting single crystals rinsed with anhydrous ethanol, and finally dried in a drying oven at 60 °C for 2h.

Synthesis of $\text{Cs}_2\text{Na}(\text{Sb}_{0.2}\text{Sc}_{0.2}\text{Er}_{0.2}\text{Yb}_{0.2}\text{Tm}_{0.2})\text{Cl}_6$ single crystals (HEA-Yb-Tm-Er)

The synthesis procedure for HEA-Er/Yb/Tm single crystals closely affinitive that of $\text{Cs}_2\text{NaReCl}_6$ single crystals. In a nutshell, 2 mmol CsCl, 1 mmol NaCl, 0.2 mmol $\text{SbCl}_3 \cdot 6\text{H}_2\text{O}$, 0.2 mmol $\text{YbCl}_3 \cdot 6\text{H}_2\text{O}$, 0.2 mmol $\text{ErCl}_3 \cdot 6\text{H}_2\text{O}$, 0.2 mmol $\text{TmCl}_3 \cdot 6\text{H}_2\text{O}$ and 0.2 mmol $\text{ScCl}_3 \cdot 6\text{H}_2\text{O}$ was blended within a 4 mL HCl solution housed in a 20 mL

stainless-steel Parr autoclave. The resulting mixture solution was subjected to a temperature of 180 °C for 12 hours, and then was slowly cooled to 25°C within 30 h.

Synthesis of $\text{Cs}_2\text{Na}(\text{Sb}_{0.2}\text{Sc}_{0.2}\text{Er}_{0.2}\text{Yb}_{0.2}\text{Ln}_{0.2})\text{Cl}_6$ single crystals (HEA-Re) ($\text{Re}^{3+}=\text{Er}^{3+}/\text{Yb}^{3+}/\text{Tm}^{3+}$)

2 mmol CsCl , 1 mmol NaCl , 0.2 mmol $\text{SbCl}_3 \cdot 6\text{H}_2\text{O}$, 0.2 mmol $\text{YCl}_3 \cdot 6\text{H}_2\text{O}$, 0.2 mmol $\text{GdCl}_3 \cdot 6\text{H}_2\text{O}$, 0.2 mmol $\text{TmCl}_3 \cdot 6\text{H}_2\text{O}$ and 0.2 mmol $\text{ScCl}_3 \cdot 6\text{H}_2\text{O}$ was blended within a 4 mL HCl solution housed in a 20 mL stainless-steel Parr autoclave. The resulting mixture solution was subjected to a temperature of 180 °C for 12 hours, and then was slowly cooled to 25°C within 30 h. The synthesis of HEA-Yb and HEA-Er single crystals are performed under otherwise identical conditions, but replaced the corresponding $\text{ReCl}_3 \cdot 6\text{H}_2\text{O}$.

Characterization: XRD measurements were performed on a SmartLab-SE X-Ray diffractometer ($\text{Cu K}\alpha$, $\lambda = 1.5406 \text{ \AA}$). SEM images and EDS mapping were captured using a field-emission scanning electron microscope (Gemini SEM 300) equipped with an Energy Dispersive Spectrometer (EDS). The selected-area electron diffraction (SAED) and high-resolution transmission electron microscopes (HRTEM) images were obtained with a JEOL JEM-ARM200F transmission electron micro scope operating at an acceleration voltage of 200 kV. X-ray photoelectron spectroscopy (XPS) data were collected using a Thermo SCIENTIFIC ESCALAB 250Xi spectrometer equipped with an $\text{Al K}\alpha$ (1486.6 eV) line as excitation source. Inductively coupled plasma mass-spectrometry (ICP-MS) was performed on a Thermo iCAP Qc. Absorption spectra were collected using a Shimadzu UV-3600 UV/Vis/NIR spectrophotometer. Photoluminescence (PL) and photoluminescence excitation (PLE) spectra were recorded by a QM8000 HORIBA spectrometer. Notably, the long pass filter of 850 nm should be applied during the measurement of NIR spectra. The PL decay curves were obtained by a time-correlated single-photon counting (TCSPC) lifetime spectroscopy system with a SpectraLED (340 nm) as the light source. Photographs for the NIR LEDs were captured by taken by an industrial night-vision camera (MVCA050-20GN,

Hikvision, China). The electroluminescence (EL) performance was measured by a fiber spectrophotometer (NIR17S spectrometer, Idea Optics, China) in the spectral region from 850 nm to 1600 nm.

Preparation of LED devices: NIR LEDs were fabricated by integrating UV LED chips ($\lambda_{\text{ex}} = 340$ nm, Shenzhen Fangpu photoelectric Co., LTD, China; FOVNNBFZ1.8W320) with HEA-Er³⁺/Yb³⁺/Tm³⁺ perovskite materials. Typically, epoxy resin A and B were weighed with a ratio of 4: 1, and then perovskite material was thoroughly mixed with epoxy resin. The mixture was then spread on surface of the UV chips and transferred in the oven followed by drying at 100 °C for 40 min to produce the NIR LED devices. The electroluminescence performance of NIR-LEDs was operated under a voltage of 3 V and currents at 100 mA.

Computational Methodology: All density functional theory (DFT) calculations were performed using the Vienna Ab initio Simulation Package (VASP).⁵⁵ The projector augmented-wave (PAW) pseudopotentials were used to treat the electron-ion interactions.⁵⁶ The generalized gradient approximation (GGA) in the Perdew–Burke–Ernzerhof (PBE) form was employed as the exchange-correlation functional to handle the interactions between electrons.⁵⁷ The unit cell of the pure-phase double perovskite studied in this work contains 40 atoms, and a $2 \times 2 \times 2$ supercell of 320 atoms was constructed to obtain a high-entropy perovskite structure with random distribution of rare-earth elements in a sublattice. Due to the inherent limitations of conventional Density Functional Theory (DFT) in dealing with localized strongly correlated electrons (e.g., the 4f orbitals of rare-earth elements), in this work, we applied the Hubbard U correction proposed by Dudarev et al.⁵⁸ to the f localized orbitals of rare-earth elements (Er, Tm, Yb) based on conventional DFT functionals, and considered on-site Coulomb interactions on the d orbitals of Er, Tm, and Yb with effective values of U = 6.5, 7.0, 6.5 eV and J = 0.8, 0.9, 0.8 eV, respectively. This introduces electron correlation energy, compensates for the aforementioned shortcomings, and makes the computational results more consistent with experiments. The plane-wave cutoff energy

was set to 342 eV. The convergence criteria were set to 10^{-5} eV for the total energy and 0.01 eV \AA^{-1} for the force, respectively. For pure-phase double perovskites, a $3 \times 3 \times 3$ Γ -centered Monkhorst–Pack k-point grid was used to sample the Brillouin zone in both geometry optimization and electronic structure calculations (including band structure, total density of states, and projected density of states). For high-entropy perovskites, due to the large supercell, only Γ point was used to sample the Brillouin zone in both geometry optimization and electronic structure calculations. The hybrid functional of Heyd–Scuseria–Ernzerhof (HSE06) was employed to obtain more accurate bandgaps based on the PBE relaxed structures.⁵⁹

Acknowledgements

This work was financially supported by the National Natural Science Foundation of China (22305089), Guangdong Provincial Basic and Applied Basic Research Fund (2025-2027) and Education Open Topics Program (2024-6) funded by the State Key Laboratory of Inorganic Synthesis and Preparative Chemistry (Jilin University). This work was also financially supported by the Fund from Science, Technology and Innovation Commission of Shenzhen Municipality (JCYJ20190809180013252), Instrument and Equipment Open Sharing Fund Project of Huazhong University of Science and Technology (No. KFGX2025018), the Key Research and Development Program of Hubei Province (YFXM2020000188), Shenzhen University Introduced Teacher Research Start-Up Project (2019012), and Natural Science Foundation of Jiangxi Province (20212BAB212014). The authors acknowledge Dr. Xiaoli Gao of the Chemical Experimental Teaching Center, School of Chemistry and Chemical Engineering, Huazhong University of Science and Technology for her assistance with morphology measurement by Scanning Electron Microscopy (SEM Hitachi SU8010). We acknowledge the Analytic & Testing Center (HUST) for Materials Characterizations. The computation is completed in the HPC Platform of Huazhong University of Science and Technology.

Conflict of Interest

The authors declare no conflict of interest.

Data Availability Statement

The data that support the findings of this study are available from the corresponding author upon reasonable request.

References

1. Liang, J.; Cao, G.; Zeng, M.; Fu, L., Controllable synthesis of high-entropy alloys. *Chemical Society Reviews* **2024**, *53* (12), 6021-6041.
2. Yao, Y.; Dong, Q.; Brozena, A.; Luo, J.; Miao, J.; Chi, M.; Wang, C.; Kevrekidis, I. G.; Ren, Z. J.; Greeley, J.; Wang, G.; Anapolsky, A.; Hu, L., High-entropy nanoparticles: Synthesis-structure-property relationships and data-driven discovery. *Science* **376** (6589), eabn3103.
3. Folgueras, M. C.; Jiang, Y.; Jin, J.; Yang, P., High-entropy halide perovskite single crystals stabilized by mild chemistry. *Nature* **2023**, *621* (7978), 282-288.
4. Song, Y.; Lan, S.; Yang, B.; Zheng, Y.; Zhou, Z.; Nan, C.-W.; Lin, Y.-H., High-Entropy Design for 2D Halide Perovskite. *Journal of the American Chemical Society* **2024**, *146* (29), 19748-19755.
5. Tian, Y.; Zhang, X.; Zhao, K.; Miao, X.; Deng, T.; Fan, W.; Jin, D.; Jiang, X.; Zhong, S.; Wang, X.; Wang, S.; Shi, P.; Tian, L.; Yao, L.; Gong, S.; Yu, X.; Gao, X.; Chen, Z.; Chen, X.; Lu, Y.; Shrote, V.; Yang, Y.; Yang, D.; Wang, R.; Xue, J., High-entropy hybrid perovskites with disordered organic moieties for perovskite solar cells. *Nature Photonics* **2024**, *18* (9), 960-966.
6. Guo, J.; Fu, Y.; Zheng, W.; Xie, M.; Huang, Y.; Miao, Z.; Han, C.; Yin, W.; Zhang, J.; Yang, X.; Tian, J.; Zhang, X., Entropy-Driven Strongly Confined Low-Toxicity Pure-Red Perovskite Quantum Dots for Spectrally Stable Light-Emitting Diodes. *Nano Letters* **2024**, *24* (1), 417-423.
7. Solari, S. F.; Poon, L.-N.; Wörle, M.; Krumeich, F.; Li, Y.-T.; Chiu, Y.-C.; Shih, C.-J., Stabilization of Lead-Reduced Metal Halide Perovskite Nanocrystals by High-Entropy Alloying. *Journal of the American Chemical Society* **2022**, *144* (13), 5864-5870.
8. Zhang, L.; Chen, Y.; Zheng, Z.; Zhou, Y.; Li, C.; Li, G.; Ren, B.; Hu, Z.; Zhou, H.; Ren, F.; Ke, W.; Fang, G., Rapid Room Temperature Entropy-Stabilized Synthesis Enabling Super-Stable Metal Halide Perovskite Semiconductor Colloidal Nanocrystals. *Advanced Functional Materials* **2025**, *n/a* (*n/a*), 2423450.

9. Chiang, Y.-T.; Shivarudraiah, S. B.; Wieczorek, A.; Khoo, K. H.; Leong, Z.; Lim, J. W. M.; Xing, Z.; Kumar, S.; Solari, S. F.; Li, Y.-T.; Chiu, Y.-C.; Sum, T. C.; Liu, Y.; Siol, S.; Shih, C.-J., Understanding Optical Properties and Electronic Structures of High-Entropy Alloyed Perovskite Nanocrystals. *Angewandte Chemie International Edition* **2025**, *64* (37), e202505890.
10. Xue, J.; Luo, J.; Chang, K. T.; Sun, Z.; Zhu, Z.; Mao, L.; Lu, H., High-Entropy Double Perovskites with Tailored Multichannel Luminescence. *Journal of the American Chemical Society* **2025**, *147* (51), 47764-47772.
11. Li, H.; Li, K.; Li, Z.; Fu, X.; Yang, Q.; Wang, N.; Wang, X.; Feng, J.; Song, S.; Zhang, H., Lanthanide-based metal halides prepared at room temperature by recrystallization method for X-ray imaging. *Light: Science & Applications* **2025**, *14* (1), 195.
12. Tan, S.; Yavuz, I.; De Marco, N.; Huang, T.; Lee, S.-J.; Choi, C. S.; Wang, M.; Nuryyeva, S.; Wang, R.; Zhao, Y.; Wang, H.-C.; Han, T.-H.; Dunn, B.; Huang, Y.; Lee, J.-W.; Yang, Y., Steric Impediment of Ion Migration Contributes to Improved Operational Stability of Perovskite Solar Cells. *Advanced Materials* **2020**, *32* (11), 1906995.
13. Li, X.; Shen, X.; Lu, M.; Wu, J.; Zhong, Y.; Wu, Z.; Yu, W. W.; Gao, Y.; Hu, J.; Zhu, J.; Zhang, Y.; Bai, X., Wide-coverage and Efficient NIR Emission from Single-component Nanophosphors through Shaping Multiple Metal-halide Packages. *Angewandte Chemie International Edition* **2023**, *62* (14), e202217832.
14. Jin, S.; Li, R.; Huang, H.; Jiang, N.; Lin, J.; Wang, S.; Zheng, Y.; Chen, X.; Chen, D., Compact ultrabroadband light-emitting diodes based on lanthanide-doped lead-free double perovskites. *Light: Science & Applications* **2022**, *11* (1), 52.
15. Liu, D.; Li, G.; Dang, P.; Zhang, Q.; Wei, Y.; Lian, H.; Shang, M.; Lin, C. C.; Lin, J., Simultaneous Broadening and Enhancement of Cr³⁺ Photoluminescence in LiIn₂SbO₆ by Chemical Unit Cosubstitution: Night-Vision and Near-Infrared Spectroscopy Detection Applications. *Angewandte Chemie International Edition* **2021**, *60* (26), 14644-14649.
16. Cho, M.-Y.; Kim, S.; Kim, I.-S.; Kim, E.-S.; Wang, Z.-J.; Kim, N.-Y.; Kim, S.-W.; Oh, J.-M., Perovskite-Induced Ultrasensitive and Highly Stable Humidity Sensor Systems Prepared by Aerosol Deposition at Room Temperature. *Advanced Functional Materials* **2020**, *30* (3), 1907449.
17. Cho, H.; Kim, Y.-H.; Wolf, C.; Lee, H.-D.; Lee, T.-W., Improving the Stability of

Metal Halide Perovskite Materials and Light-Emitting Diodes. *Advanced Materials* **2018**, *30* (42), 1704587.

18. Kim, H.; Yoo, S.-M.; Ding, B.; Kanda, H.; Shibayama, N.; Syzgantseva, M. A.; Tirani, F. F.; Schouwink, P.; Yun, H. J.; Son, B.; Ding, Y.; Kim, B.-S.; Kim, Y. Y.; Park, J.; Syzgantseva, O. A.; Jeon, N. J.; Dyson, P. J.; Nazeeruddin, M. K., Shallow-level defect passivation by 6H perovskite polytype for highly efficient and stable perovskite solar cells. *Nature Communications* **2024**, *15* (1), 5632.
19. Karan, N. S.; Banerjee, S.; Tripathi, A.; Ghosh, S.; Das, R.; Pandit, R.; Das, A.; Mukherjee, S.; Adarsh, K. V.; Mandal, P. K.; Pradhan, N., Beyond Surface Facets and Morphology: Precision Silica Shelling for Enhanced Luminescence and Stability in Halide Perovskite Nanocrystals. *Journal of the American Chemical Society* **2025**, *147* (49), 45043-45056.
20. Hua, Y.; Zhang, G.; Sun, X.; Zhang, P.; Hao, Y.; Xu, Y.; Yang, Y.; Lin, Q.; Li, X.; Zhai, Z.; Cui, F.; Liu, H.; Liu, J.; Tao, X., Suppressed ion migration for high-performance X-ray detectors based on atmosphere-controlled EFG-grown perovskite CsPbBr_3 single crystals. *Nature Photonics* **2024**, *18* (8), 870-877.
21. Samatov, M. R.; Liu, D.; Zhao, L.; Kazakova, E. A.; Abrameshin, D. A.; Das, A.; Vasenko, A. S.; Prezhdo, O. V., Ion Migration at Metal Halide Perovskite Grain Boundaries Elucidated with a Machine Learning Force Field. *The Journal of Physical Chemistry Letters* **2024**, *15* (50), 12362-12369.
22. Liu, X.; Fang, Q.; Yang, Z.; Zhou, J.; Yan, Z.; Nie, S.; Ju, M.-G.; Wang, J.; Deng, Z., High-Entropy Lead-Free Organic–Inorganic Hybrid Perovskites Exhibiting Broad Absorption and Bright Golden Emission for LEDs. *Angewandte Chemie International Edition* **2025**, *n/a* (*n/a*), e16911.
23. Luo, J.; Wang, X.; Li, S.; Liu, J.; Guo, Y.; Niu, G.; Yao, L.; Fu, Y.; Gao, L.; Dong, Q.; Zhao, C.; Leng, M.; Ma, F.; Liang, W.; Wang, L.; Jin, S.; Han, J.; Zhang, L.; Etheridge, J.; Wang, J.; Yan, Y.; Sargent, E. H.; Tang, J., Efficient and stable emission of warm-white light from lead-free halide double perovskites. *Nature* **2018**, *563* (7732), 541-545.
24. Jia, Y. Q., Crystal radii and effective ionic radii of the rare earth ions. *Journal of Solid State Chemistry* **1991**, *95* (1), 184-187.
25. Zhou, B.; Fang, F.; Liu, Z.; Zhong, H.; Zhou, K.; Hu, H.; Min, J.; Zheng, F.; Fang, S.; Nie, J.; Huang, J.-K.; Li, L.-J.; Li, H.; Wan, Y.; Shi, Y., Self-Trapped Exciton Emission in Highly Polar 0D Hybrid Ammonium/Hydronium-Based Perovskites

Triggered by Antimony Doping. *Journal of the American Chemical Society* **2024**, *146* (22), 15198-15208.

26. Cai, T.; Shi, W.; Hwang, S.; Kobbekaduwa, K.; Nagaoka, Y.; Yang, H.; Hills-Kimball, K.; Zhu, H.; Wang, J.; Wang, Z.; Liu, Y.; Su, D.; Gao, J.; Chen, O., Lead-Free $\text{Cs}_4\text{CuSb}_2\text{Cl}_{12}$ Layered Double Perovskite Nanocrystals. *Journal of the American Chemical Society* **2020**, *142* (27), 11927-11936.
27. López-Mena, E. R.; Ceballos-Sánchez, O.; Hooper, T. J. N.; Sanchez-Ante, G.; Rodríguez-Muñoz, M.; Renteria-Salcedo, J. A.; Elías-Zuñiga, A.; Sanchez-Martinez, A., The effect of Yb doping on ZnO thin films obtained via a low-temperature spin coating method. *Journal of Materials Science: Materials in Electronics* **2021**, *32* (1), 347-359.
28. Huynh, T. V.; Anh, N. T. N.; Darmanto, W.; Doong, R.-A., Erbium-doped graphene quantum dots with up- and down-conversion luminescence for effective detection of ferric ions in water and human serum. *Sensors and Actuators B: Chemical* **2021**, *328*, 129056.
29. Wang, M.; Chen, X.; Zhang, F.; Ma, Z.; Ji, X.; Cheng, S.; Pan, G.; Wu, D.; Li, X.-J.; Zhang, Y.; Shan, C.; Shi, Z., Colloidal Synthesis of Blue-Emitting Cs_3TmCl_6 Nanocrystals via Localized Excitonic Recombination for Down-Conversion White Light-Emitting Diodes. *ACS Nano* **2024**, *18* (44), 30421-30432.
30. Kabongo, G. L.; Mhlongo, G. H.; Mothudi, B. M.; Hillie, K. T.; Mbule, P. S.; Dhlamini, M. S., Structural, photoluminescence and XPS properties of Tm^{3+} ions in ZnO nanostructures. *Journal of Luminescence* **2017**, *187*, 141-153.
31. Hsu, W.-L.; Tsai, C.-W.; Yeh, A.-C.; Yeh, J.-W., Clarifying the four core effects of high-entropy materials. *Nature Reviews Chemistry* **2024**, *8* (6), 471-485.
32. Krawczyk, P. A.; Jurczyszyn, M.; Pawlak, J.; Salamon, W.; Baran, P.; Kmita, A.; Gondek, Ł.; Sikora, M.; Kapusta, C.; Strączek, T.; Wyrwa, J.; Żywczałk, A., High-Entropy Perovskites as Multifunctional Metal Oxide Semiconductors: Synthesis and Characterization of $(\text{Gd}_{0.2}\text{Nd}_{0.2}\text{La}_{0.2}\text{Sm}_{0.2}\text{Y}_{0.2})\text{CoO}_3$. *ACS Applied Electronic Materials* **2020**, *2* (10), 3211-3220.
33. Liu, Y.; Tu, D.; Yang, M.; Li, H.; Li, C.; Xie, Z.; Zhou, S.; Yu, S.; Xu, J.; Chen, X., Near-Infrared and Visible Dual-Band Self-Trapped Exciton Emissions from Li+-Doped $\text{Cs}_2\text{NaScCl}_6$ Double Perovskites. *ACS Energy Letters* **2025**, *10* (5), 2150-2159.
34. Pan, E.; Bai, G.; Zhou, J.; Lei, L.; Xu, S., Exceptional modulation of upconversion and downconversion near-infrared luminescence in Tm/Yb-codoped ferroelectric

nanocomposite by nanoscale engineering. *Nanoscale* **2019**, *11* (24), 11642-11648.

35. Rao, Z.; Li, Z.; Zhao, X.; Gong, X., Targeted high-precision up-converting thermometer platform over multiple temperature zones with Er^{3+} . *Materials Horizons* **2023**, *10* (5), 1816-1824.

36. Lian, B.; Hou, H.; Lin, F.; Luo, B.; Pan, D.; Zou, B.; Zeng, R., Multimode Luminescence with Temperature and Energy Level Synergistic Dependence in Rare Earth Halide DPs for Advanced Multifunctional Applications. *Small* **2024**, *20* (35), 2401093.

37. Xin, Y.; Wang, J.; Gao, X.; Yang, Y.; Zhang, J.; Tang, J.; Zhang, Z., Ultrabroadband (Vis-NIR) Emission in Single-Component Perovskite LEDs via Tailored Multi-Exciton Energy Transfer Pathways. *Advanced Materials* **2025**, *n/a* (n/a), 2501658.

38. Wang, Y.; Hou, H.; Bai, Y.; Zou, B.; Zeng, R., Thermal Enhanced Energy Transfer and High Thermal Sensitivity of Sb^{3+} Doped $\text{Cs}_2\text{KYbCl}_6$ Rare Earth Double Perovskites. *Laser & Photonics Reviews* **2024**, *18* (11), 2400337.

39. Li, X.; Shen, X.; Lu, M.; Wu, J.; Zhong, Y.; Wu, Z.; Yu, W. W.; Gao, Y.; Hu, J.; Zhu, J., Wide-coverage and efficient NIR emission from single-component nanophosphors through shaping multiple metal-halide packages. *Angewandte Chemie International Edition* **2023**, *62* (14), e202217832.

40. Wang, Y.; Dang, P.; Qiu, L.; Zhang, G.; Liu, D.; Wei, Y.; Lian, H.; Li, G.; Cheng, Z.; Lin, J., Multimode luminescence tailoring and improvement of $\text{Cs}_2\text{NaHoCl}_6$ cryolite crystals via $\text{Sb}^{3+}/\text{Yb}^{3+}$ alloying for versatile photoelectric applications. *Angewandte Chemie* **2023**, *135* (45), e202311699.

41. Gao, W.; Abbas, N.; Xin, Y.; Wang, J.; Xiao, X.; Qi, Y.; Zhang, T.; Zhang, Z., Lead-Free Rare-Earth Based Halide Double Perovskites: From Fundamentals, Progress to Perspectives. *Laser & Photonics Reviews* **2025**, *n/a* (n/a), 2500113.

42. Xin, Y.; Xiao, X.; Wang, J.; Abbas, N.; Zhang, S.; Han, Y.; Tang, J.; Skripka, A.; Zhang, Z., Multi-Ion Doping in Low-Phonon-Energy Nd^{3+} Based Double Perovskite Unlocks Multimodal Anti-Counterfeiting and High-Performance Optical Thermometry. *Advanced Functional Materials* **2025**, *n/a* (n/a), e25789.

43. Tang, Y.; Pu, G.; Liu, Q.; Li, J.; Wang, X.; Suenaga, K.; Bi, H.; Chen, W.; Wang, J., Metal Halide Perovskite Enriched with Entropy-Induced Lattice Distortion for Enhanced X-ray Detection. *ACS Nano* **2025**, *19* (33), 30396-30406.

44. Gao, Z.; Mao, G.; Chen, S.; Bai, Y.; Gao, P.; Wu, C.; Gates, I. D.; Yang, W.; Ding, X.; Yao, J., High throughput screening of promising lead-free inorganic halide double

perovskites via first-principles calculations. *Physical Chemistry Chemical Physics* **2022**, *24* (5), 3460-3469.

45. Liu, B.; Li, Y.; Xu, S.; Chang, J.; Gao, Y.; Yu, H.; Wang, Y.; Chen, B., Simultaneous Improvement and Tailoring Upconversion and Downshift Luminescence of $\text{Cs}_2\text{NaErCl}_6$ via Yb^{3+} Alloying for Versatile Photoelectric Applications. *ACS Applied Materials & Interfaces* **2025**, *17* (12), 18688-18700.
46. Zhu, Y.; Pan, G.; Zhao, J.; Liu, K.; Xue, W.; Wang, Y.; You, W.; Gao, H.; Xu, W.; Mao, Y., High-Efficiency Dual-Mode Polychromatic Emission of Rare-Earth-Based Double Perovskite with Low Phonon Energy toward High-Level Anti-Counterfeiting and Information Encryption. *Advanced Optical Materials* **2023**, *11* (2), 2202019.
47. Chen, C.; Tuo, Y.; Wang, Z.; Sun, M.; Du, Y.; Han, Z.; Yun, X.; Shi, S.; Xie, J.; Gao, S.; Chen, W.; Dong, C.; Guan, X.; Liu, G.; Lu, P., Machine learning, theoretical exploration and device simulation of $\text{Cs}_2\text{NaXCl}_6$ (X=Bi, In, Sb, Sc) double halide perovskites with spatial applications. *Solar Energy* **2025**, 287, 113199.
48. Wang, B.-F.; Yu, Y.; Shen, Y.; Wu, Y.-H.; Su, Z.-H.; Wang, Y.-T.; Zhang, Y.-H.; Cao, L.-X.; Gao, X.-Y.; Tang, J.-X.; Li, Y.-Q., Enhanced Electroluminescence and Stability of Sky-Blue Perovskite Light-Emitting Diodes. *Angewandte Chemie International Edition* **2025**, *64* (11), e202419746.
49. Chi, W.; Banerjee, S. K., Achieving Resistance against Moisture and Oxygen for Perovskite Solar Cells with High Efficiency and Stability. *Chemistry of Materials* **2021**, *33* (12), 4269-4303.
50. Liu, D.; Dang, P.; Zhang, G.; Lian, H.; Li, G.; Lin, J., Near-infrared emitting metal halide materials: Luminescence design and applications. *InfoMat* **2024**, *6* (5), e12542.
51. Liu, Y.; Di Stasio, F.; Bi, C.; Zhang, J.; Xia, Z.; Shi, Z.; Manna, L., Near-Infrared Light Emitting Metal Halides: Materials, Mechanisms, and Applications. *Advanced Materials* **2024**, *36* (21), 2312482.
52. Dang, P.; Zhang, G.; Yang, W.; Lian, H.; Li, G.; Lin, J., Red–NIR luminescence in rare-earth and manganese ions codoped $\text{Cs}_4\text{CdBi}_2\text{Cl}_{12}$ vacancy-ordered quadruple perovskites. *Chemistry of Materials* **2023**, *35* (4), 1640-1650.
53. Liu, B.-M.; Guo, X.-X.; Huang, L.; Zhou, R.-F.; Zou, R.; Ma, C.-G.; Wang, J., A Super-Broadband NIR Dual-Emitting $\text{Mg}_2\text{SnO}_4:\text{Cr}^{3+},\text{Ni}^{2+}$ Phosphor for Ratiometric Phosphor-Converted NIR Light Source Applications. *Advanced Materials Technologies* **2023**, *8* (4), 2201181.
54. Chen, W.; Huang, X.; Dong, Q.; Zhou, Z.; Xiong, P.; Le, Y.; Song, E.; Qiu, J.; Yang,

Z.; Dong, G., Thermally stable and tunable broadband near-infrared emission from NIR-I to NIR-II in Bi-doped germanate glass for smart light sources. *Journal of Materials Chemistry C* **2023**, *11* (3), 953-962.

55. Kresse, G.; Furthmüller, J., Efficiency of ab-initio total energy calculations for metals and semiconductors using a plane-wave basis set. *Computational Materials Science* **1996**, *6* (1), 15-50.

56. Kresse, G.; Joubert, D., From ultrasoft pseudopotentials to the projector augmented-wave method. *Physical Review B* **1999**, *59* (3), 1758-1775.

57. Perdew, J. P.; Burke, K.; Ernzerhof, M., Generalized Gradient Approximation Made Simple. *Physical Review Letters* **1996**, *77* (18), 3865-3868.

58. Dudarev, S. L.; Botton, G. A.; Savrasov, S. Y.; Humphreys, C. J.; Sutton, A. P., Electron-energy-loss spectra and the structural stability of nickel oxide: An LSDA+U study. *Physical Review B* **1998**, *57* (3), 1505-1509.

59. Heyd, J.; Scuseria, G. E.; Ernzerhof, M., Hybrid functionals based on a screened Coulomb potential. *The Journal of Chemical Physics* **2003**, *118* (18), 8207-8215.

Supporting Information

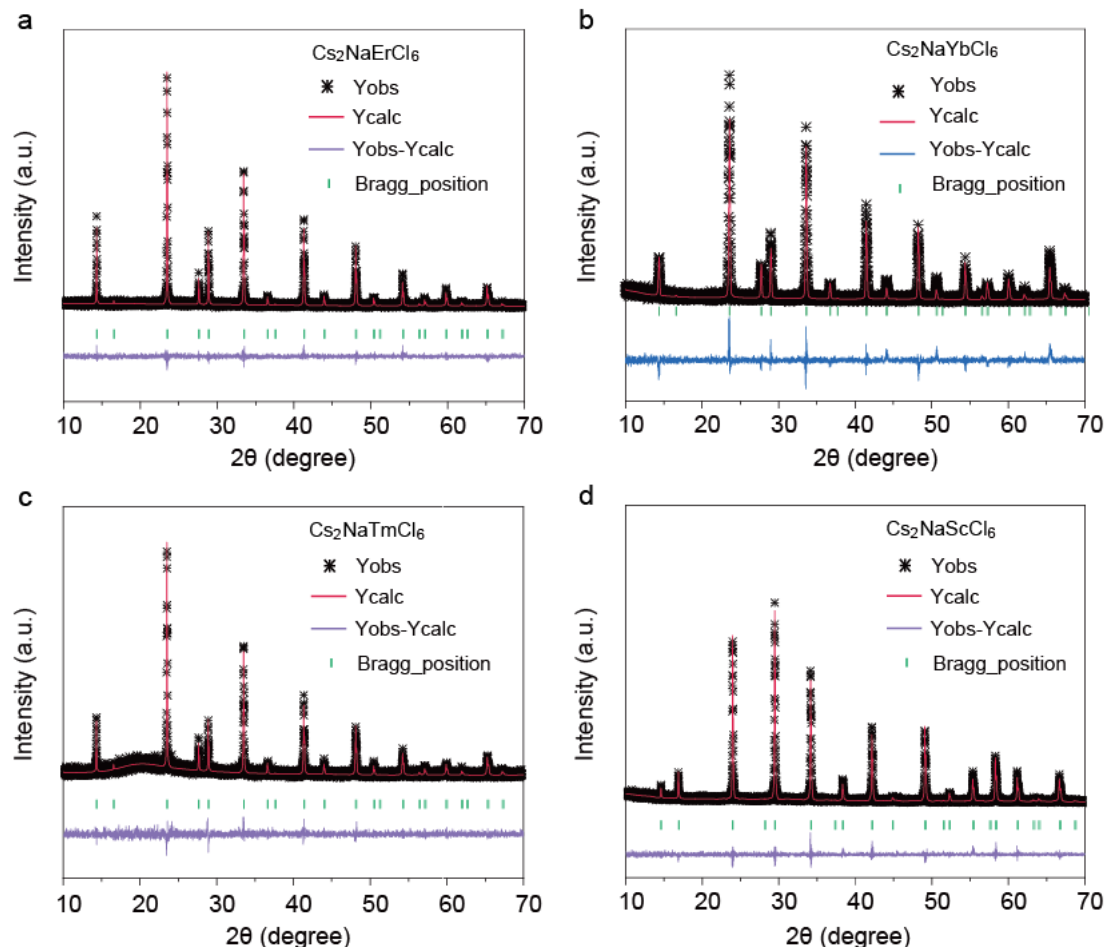


Figure S1. Rietveld refinement of XRD pattern for the $\text{Cs}_2\text{NaErCl}_6$ (a), $\text{Cs}_2\text{NaYbCl}_6$ (b), $\text{Cs}_2\text{NaTmCl}_6$ (c) and $\text{Cs}_2\text{NaScCl}_6$ (d) **single crystals**.

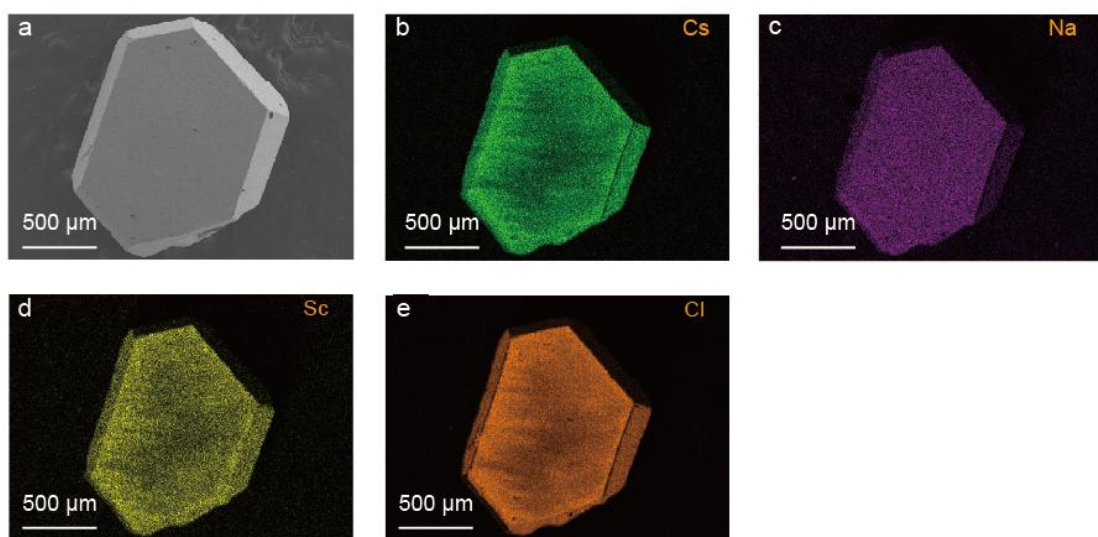


Figure S2. SEM image and EDS elemental mappings in $\text{Cs}_2\text{NaScCl}_6$ **single crystals**. Cs (b), Na (c), Sc (d) and Cl (e) elements are homogeneously distributed in the **single crystals**.

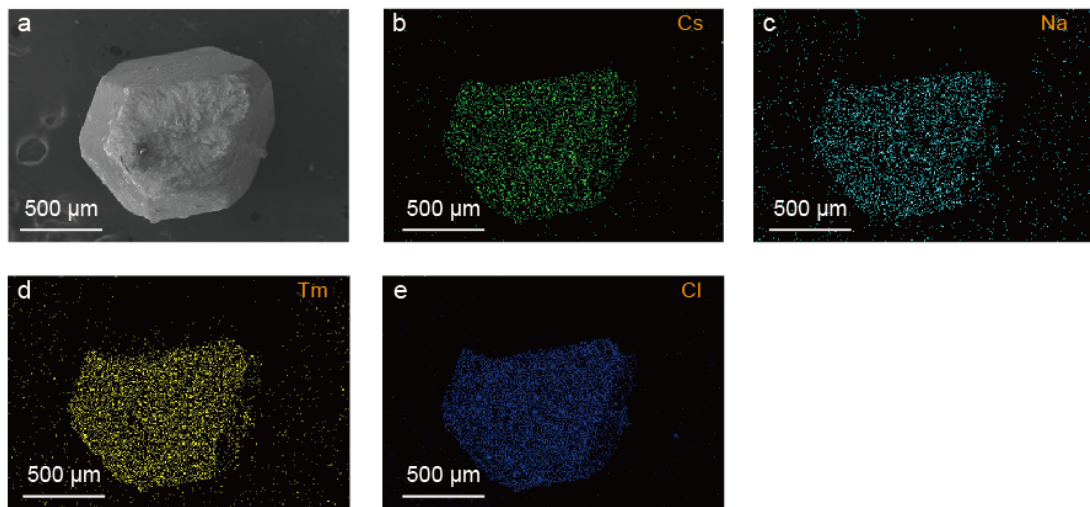


Figure S3. SEM image and EDS elemental mappings in $\text{Cs}_2\text{NaTmCl}_6$ **single crystals**. Cs (b), Na (c), Tm (d) and Cl (e) elements are homogeneously distributed in the **single crystals**.

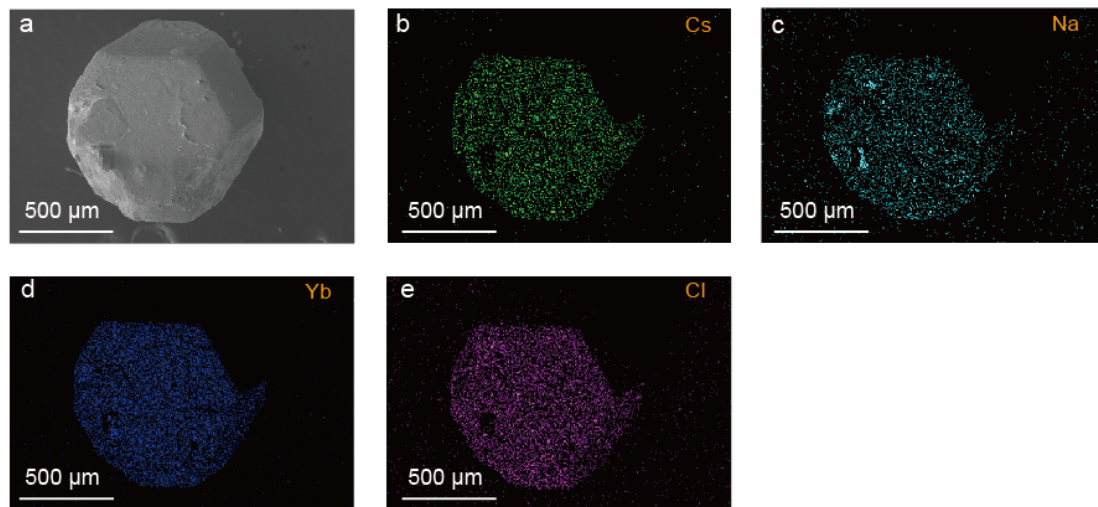


Figure S4. SEM image and EDS elemental mappings in $\text{Cs}_2\text{NaYbCl}_6$ **single crystals**. Cs (b), Na (c), Yb (d) and Cl (e) elements are homogeneously distributed in the **single crystals**.

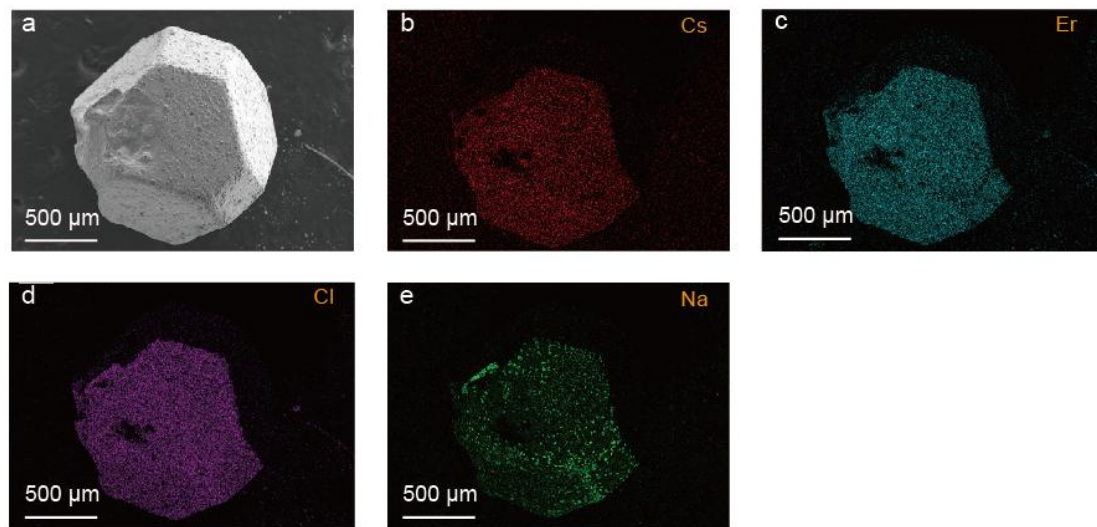


Figure S5. SEM image and EDS elemental mappings in $\text{Cs}_2\text{NaErCl}_6$ **single crystals**. Cs (b), Na (c), Er (d) and Cl (e) elements are homogeneously distributed in the **single crystals**.

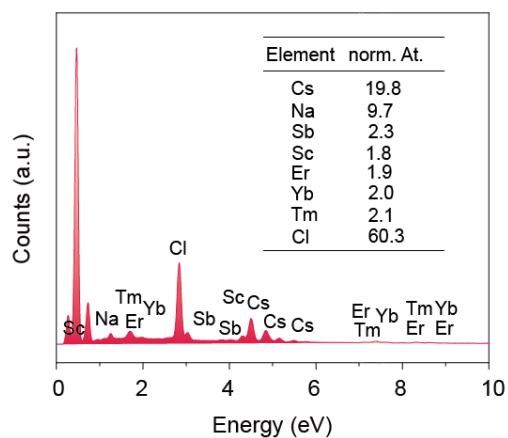


Figure S6. EDS spectrum of **HEA-Yb-Tm-Er single crystals**. Quantitative analysis from EDS reveals an atomic ratio of Cs/Na/Sb/Sc/Tm/Yb/Er/Cl at 1.98/0.97/0.23/0.18/0.21/0.2/0.19/6.03.

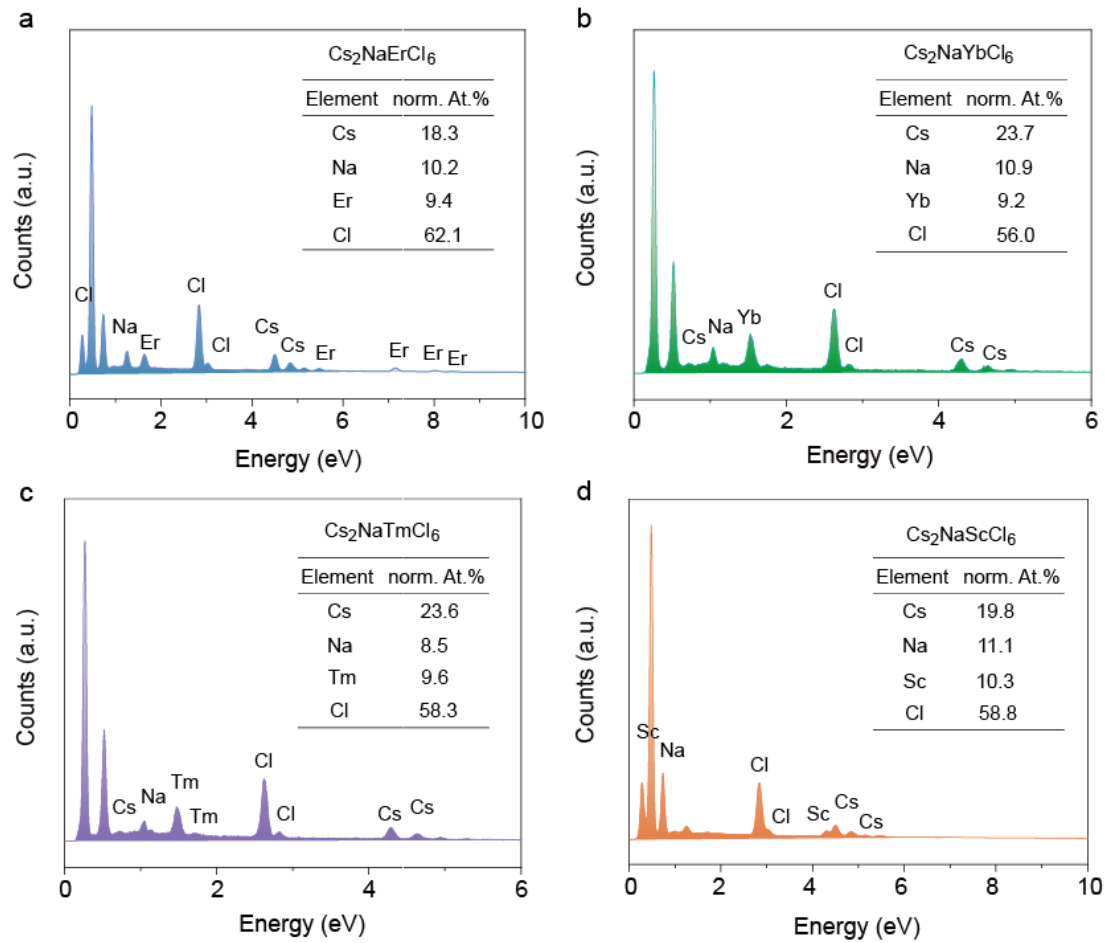


Figure S7. EDS spectrum of $\text{Cs}_2\text{NaErCl}_6$ (a), $\text{Cs}_2\text{NaYbCl}_6$ (b), $\text{Cs}_2\text{NaTmCl}_6$ (c) and $\text{Cs}_2\text{NaScCl}_6$ (d) **single crystals**. Quantitative analysis from EDS reveals an atomic ratio of Cs/Na/Re/Cl at 2/1/1/6.

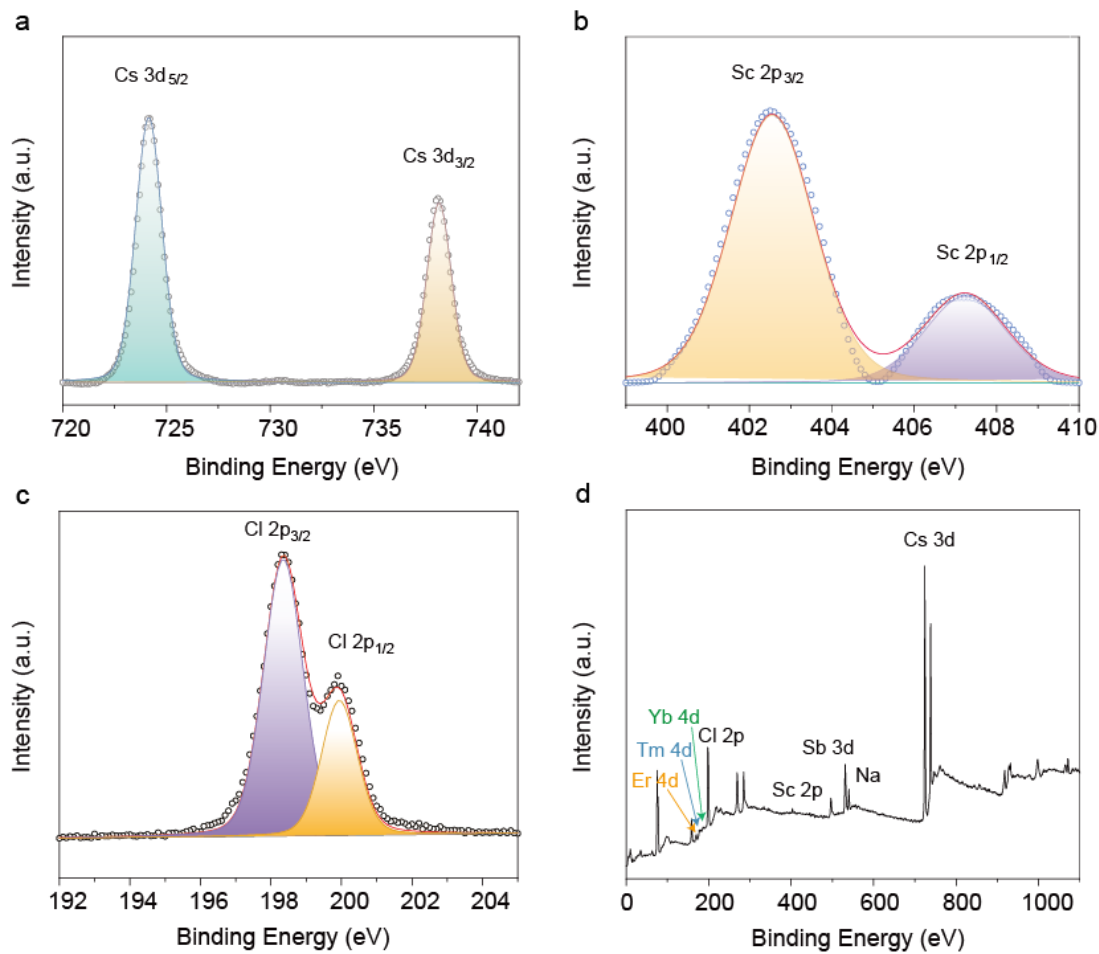


Figure S8. XPS spectra of **HEA-Yb-Tm-Er single crystals**. (a) The binding energy peaks of 724.1 and 738.1 eV are attributed to correspond to Cs 3d_{5/2} and Cs 3d_{3/2}, respectively. (b) The binding energy peaks at 402.5 and 407.2 eV are assigned to 2p_{3/2} and 2p_{1/2} of Sc³⁺. (c) The peaks at 198.3 eV and 199.9 eV correspond to Cl 2p_{3/2} and Cl 2p_{1/2}. (d) XPS survey scan spectrum. These results provide further confirmation of successful realization of **HEA-Yb-Tm-Er single crystals**.

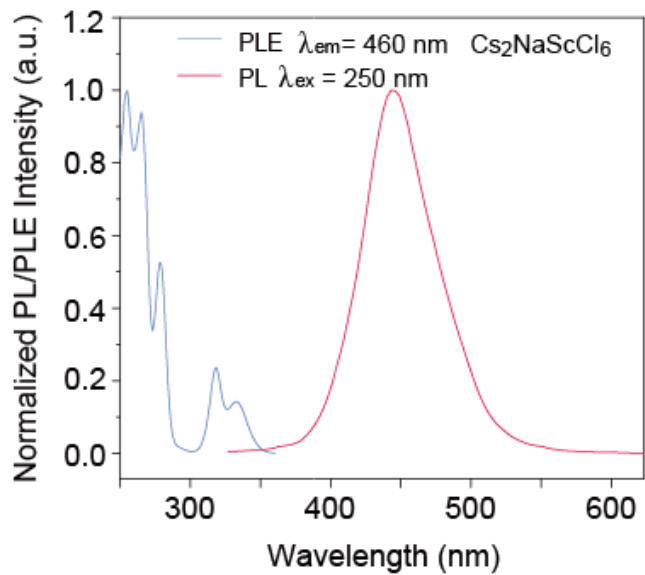


Figure S9. The normalized PLE and PL spectra of $\text{Cs}_2\text{NaScCl}_6$ single crystals.

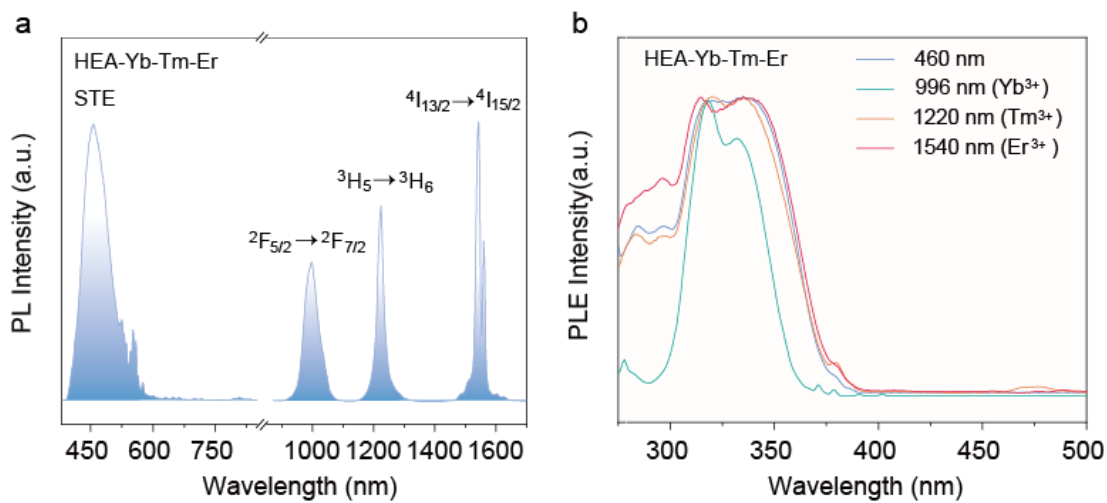


Figure S10. (a) PL spectra of **HEA-Yb-Tm-Er** single crystals. (b) PL excitation spectra monitored at Sb^{3+} emission (460 nm), Yb^{3+} (996 nm), Tm^{3+} (1220 nm), Er^{3+} (1540 nm) emissions for **HEA-Yb-Tm-Er** single crystals, respectively.

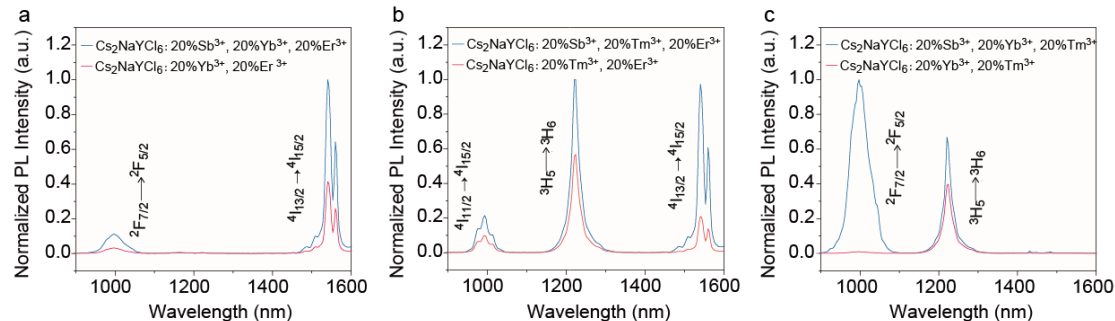


Figure S11. NIR PL spectra of $\text{Cs}_2\text{NaYCl}_6:20\%\text{Sb}^{3+}$, $20\%\text{Yb}^{3+}$, $20\%\text{Er}^{3+}$ and $\text{Cs}_2\text{NaYCl}_6: 20\%\text{Yb}^{3+}$, $20\%\text{Er}^{3+}$ (a); $\text{Cs}_2\text{NaYCl}_6:20\%\text{Sb}^{3+}$, $20\%\text{Tm}^{3+}$, $20\%\text{Er}^{3+}$ and $\text{Cs}_2\text{NaYCl}_6: 20\%\text{Tm}^{3+}$, $20\%\text{Er}^{3+}$ (b); $\text{Cs}_2\text{NaYCl}_6:20\%\text{Sb}^{3+}$, $20\%\text{Yb}^{3+}$, $20\%\text{Tm}^{3+}$ and $\text{Cs}_2\text{NaYCl}_6: 20\%\text{Yb}^{3+}$, $20\%\text{Tm}^{3+}$.

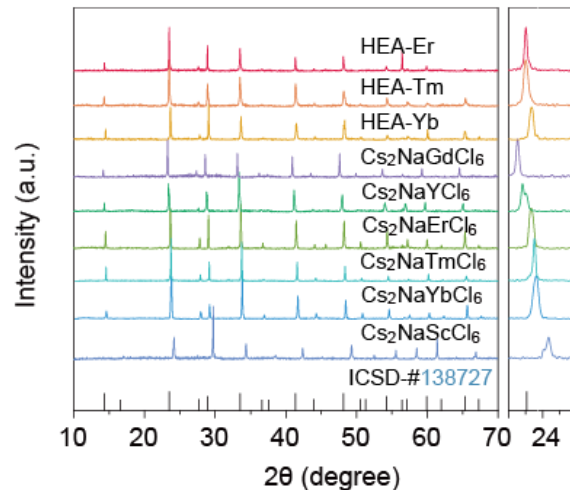


Figure S12. The XRD patterns for the HEA-Tm, HEA-Er and HEA-Yb single crystals revealed a slight shift in the diffraction peak in 2θ range of $23\text{--}25^\circ$, which was attributed to the difference of ionic radii for Re^{3+} ions.

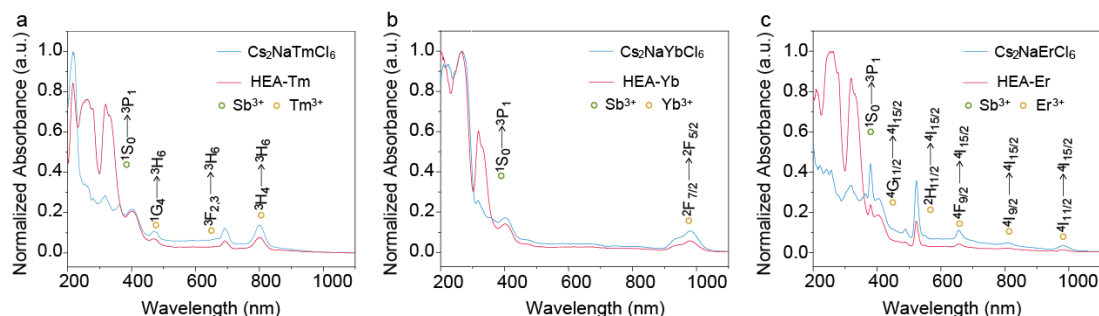
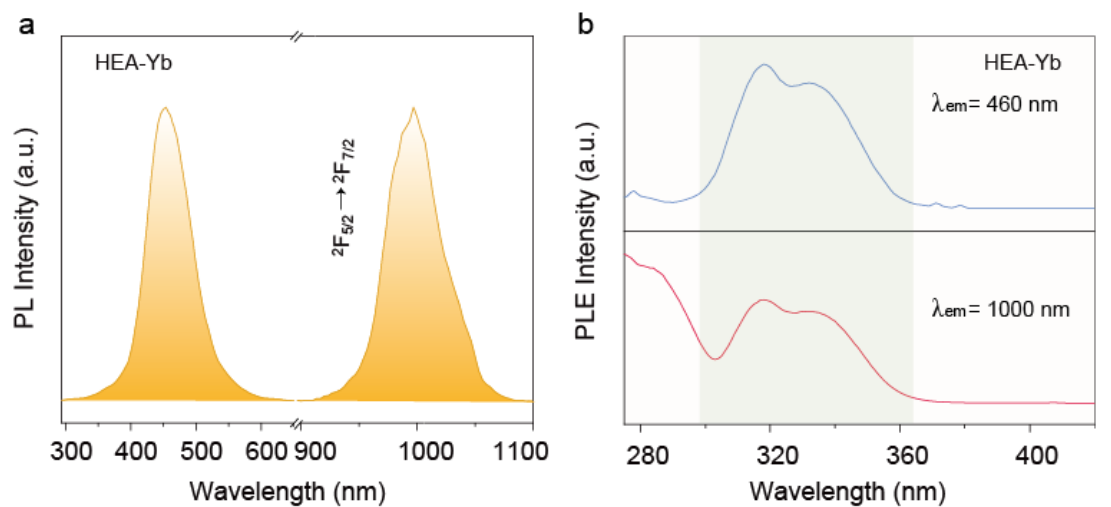
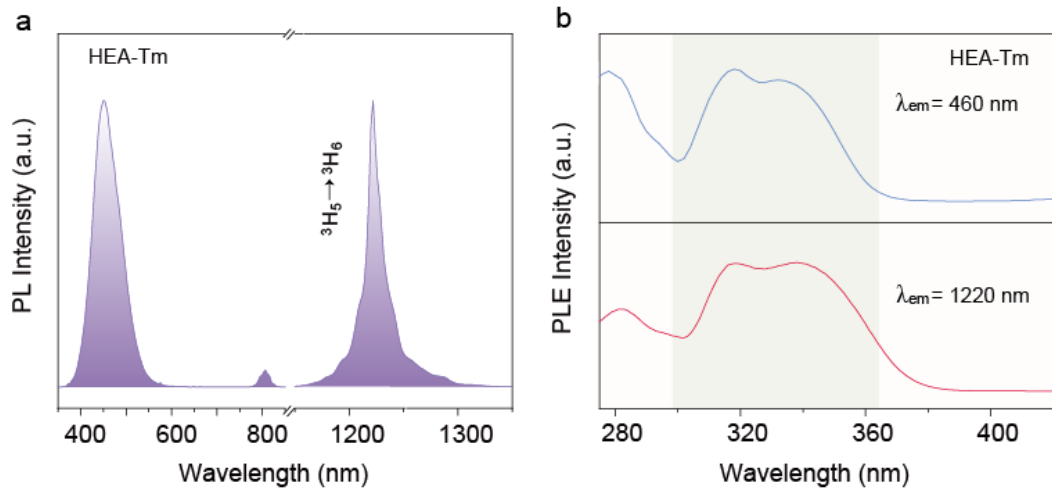


Figure S13. Absorption spectra of $\text{Cs}_2\text{NaReCl}_6$ ($\text{Re}^{3+} = \text{Tm}^{3+}$, Er^{3+} and Yb^{3+}) and HEA-Tm (a), HEA-Yb (b), HEA-Er (c).

The absorption spectra of HEA-Re ($\text{Re}^{3+} = \text{Tm}^{3+}$, Er^{3+} and Yb^{3+}) single crystals displayed the similar absorption peaks with $\text{Cs}_2\text{NaReCl}_6$ single crystals, respectively. Upon alloying, the new absorption peaks centered around at 268 nm, 282 nm and 300-380 nm, corresponding to the $^1\text{S}_0 \rightarrow ^{1,2,3}\text{P}_1$ transition of Sb^{3+} ions were observed.



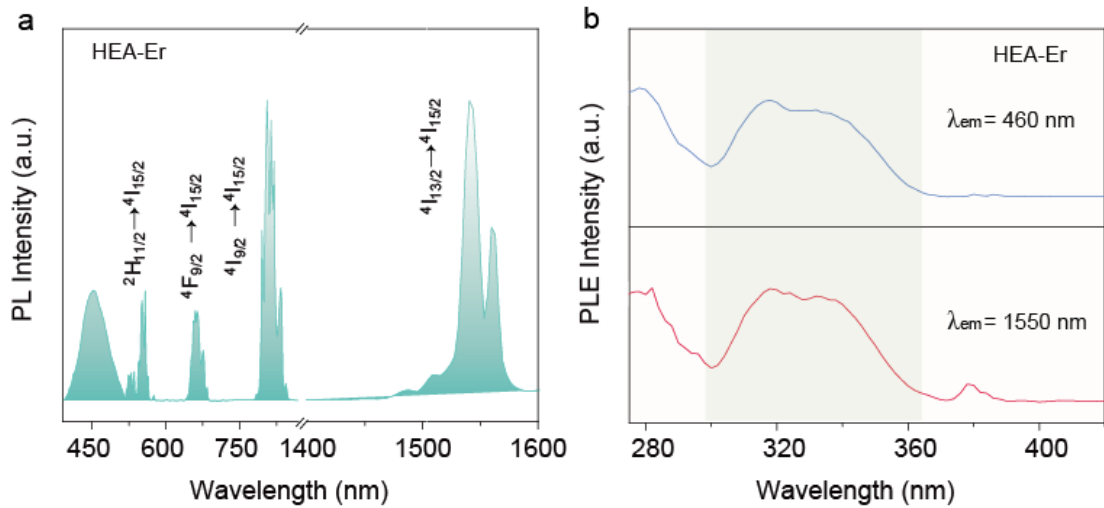


Figure S16. (a) PL spectra of **HEA-Er single crystals**. (b) PL excitation spectra monitored at Sb^{3+} (460 nm) and Er^{3+} (1540 nm) emissions for **HEA-Er single crystals**, respectively.

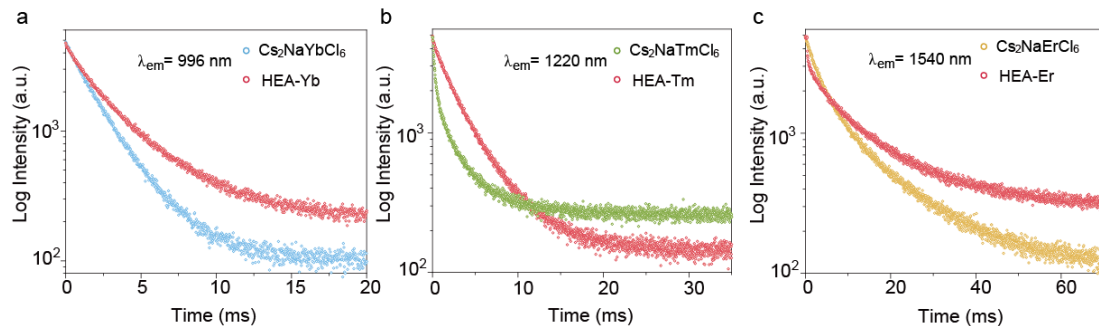


Figure S17. PL decay curves monitored at 996 nm, 1220 nm and 1540 nm for $\text{Cs}_2\text{NaReCl}_6$ ($\text{Re}^{3+} = \text{Yb}^{3+}$, Tm^{3+} and Er^{3+}) and HEA-Yb (a), HEA-Tm (b), HEA-Er (c) single crystals, respectively.

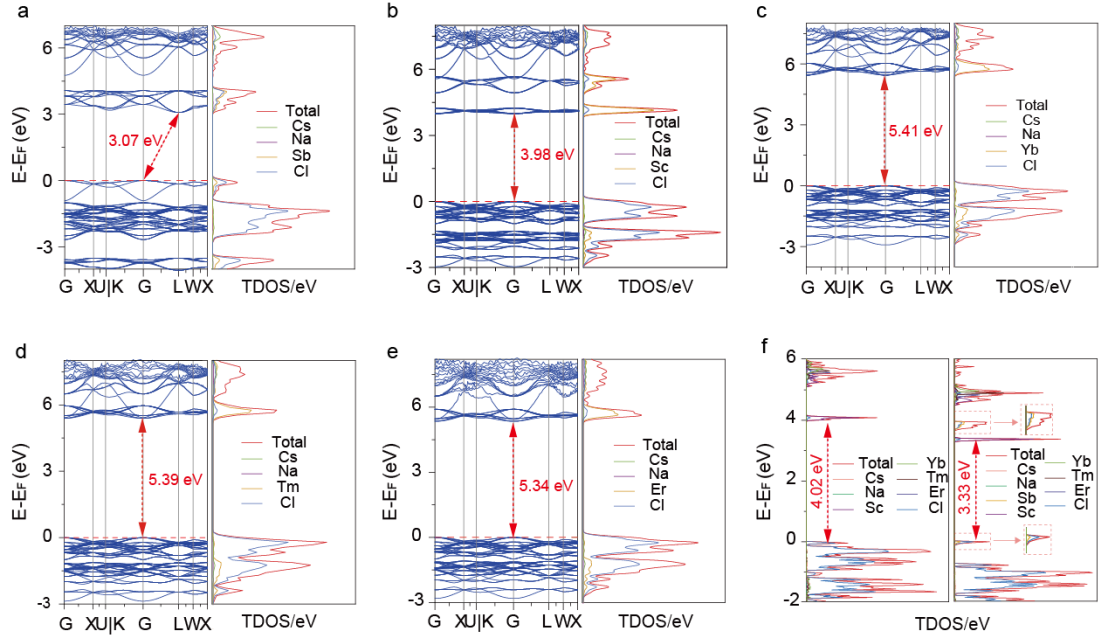


Figure S18. Electronic band structures (left panel) and the corresponding projected density of states (PDOS) (right panel) for Cs₂NaSbCl₆ (a), Cs₂NaScCl₆ (b), Cs₂NaYbCl₆ (c), Cs₂NaTmCl₆ (d) and Cs₂NaErCl₆ (e); (f) PDOS for Cs₂Na(Sc_{0.25}Yb_{0.25}Tm_{0.25}Er_{0.25})Cl₆ (left) and HEA-Yb-Tm-Er single crystals (right). These results were calculated using the DFT-PBE method.

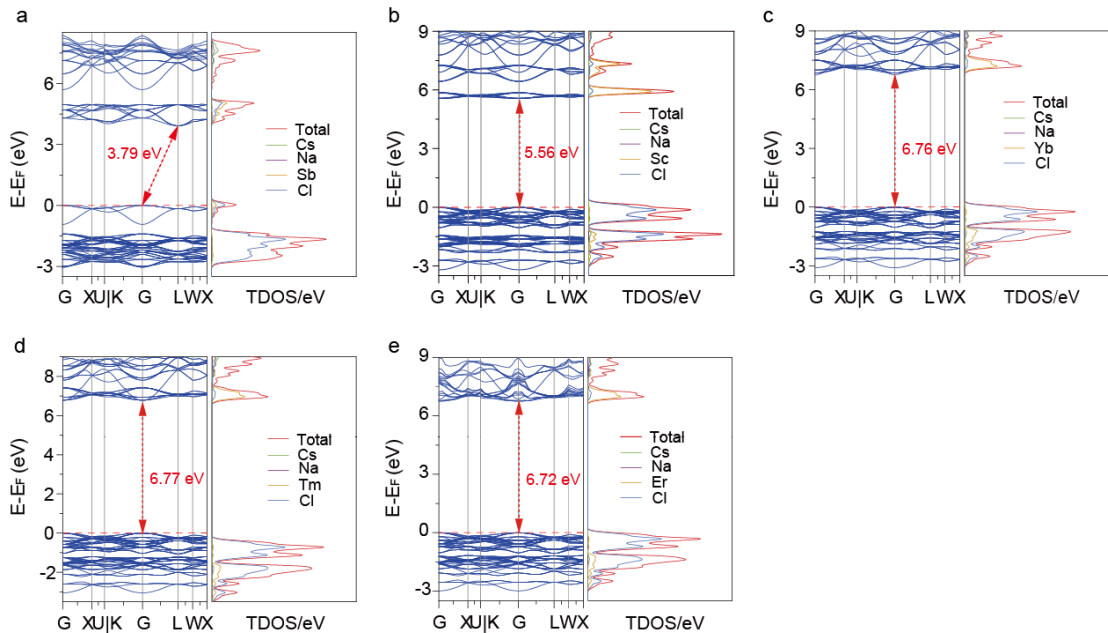


Figure S19. Electronic band structures (left panel) and the corresponding projected density of states (PDOS) (right panel) for Cs₂NaSbCl₆ (a), Cs₂NaScCl₆ (b), Cs₂NaYbCl₆ (c), Cs₂NaTmCl₆ (d) and Cs₂NaErCl₆ (e). These results were calculated using the DFT-HSE method.

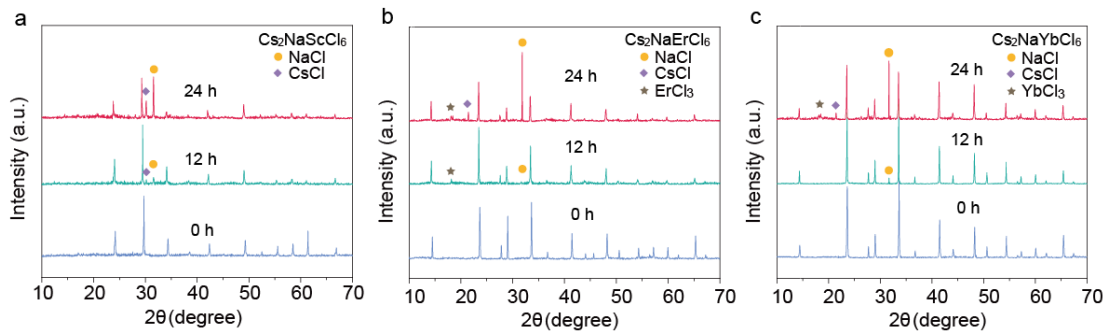


Figure S20. Humidity stability tests (100% RH, 25°C) from 0 to 24 h. XRD of $\text{Cs}_2\text{NaScCl}_6$ (a), $\text{Cs}_2\text{NaErCl}_6$ (b) and $\text{Cs}_2\text{NaYbCl}_6$ (c) single crystals.



Figure S21. Humidity stability tests (100% RH, 25°C) from 0 to 24 h. Optical microscope images of $\text{Cs}_2\text{NaScCl}_6$ single crystals.

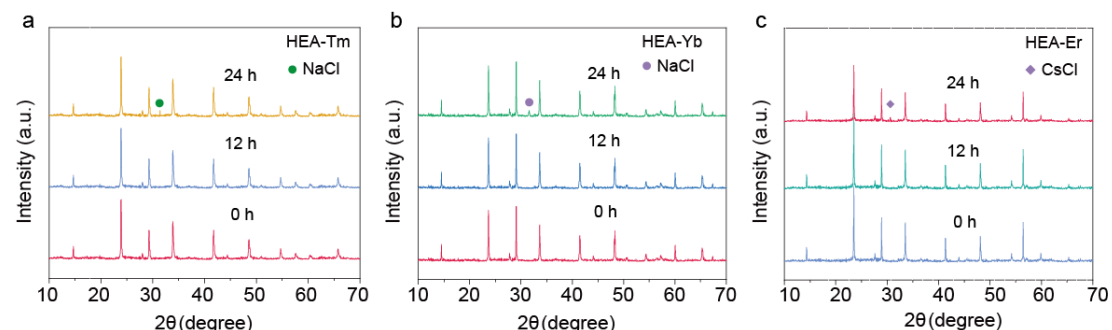


Figure S22. Humidity stability tests (100% RH, 25°C) from 0 to 24 h. XRD of HEA-Tm, HEA-Er and HEA-Yb single crystals.

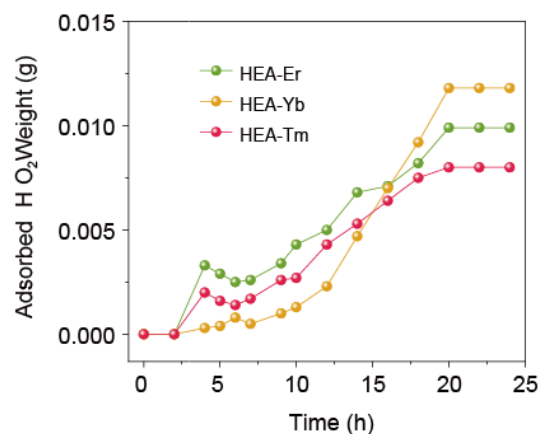


Figure S23. Humidity stability tests (100% RH, 25°C) from 0 to 24 h. Weight increased curves of HEA-Tm, HEA-Er and HEA-Yb single crystals.

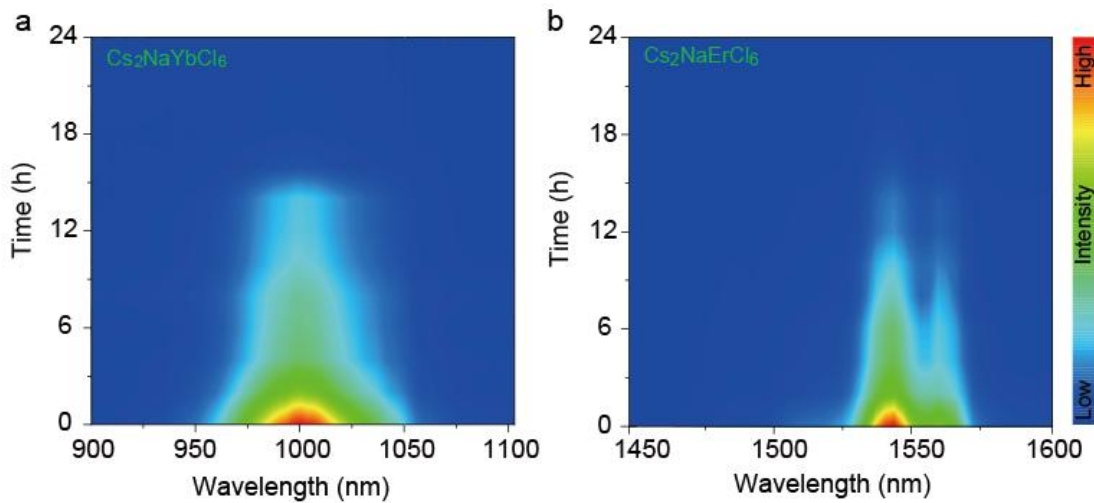


Figure S24. Humidity stability tests (100% RH, 25°C) from 0 to 24 h. NIR PL spectra of Cs₂NaYbCl₆ (a) and Cs₂NaErCl₆ (b) single crystals.

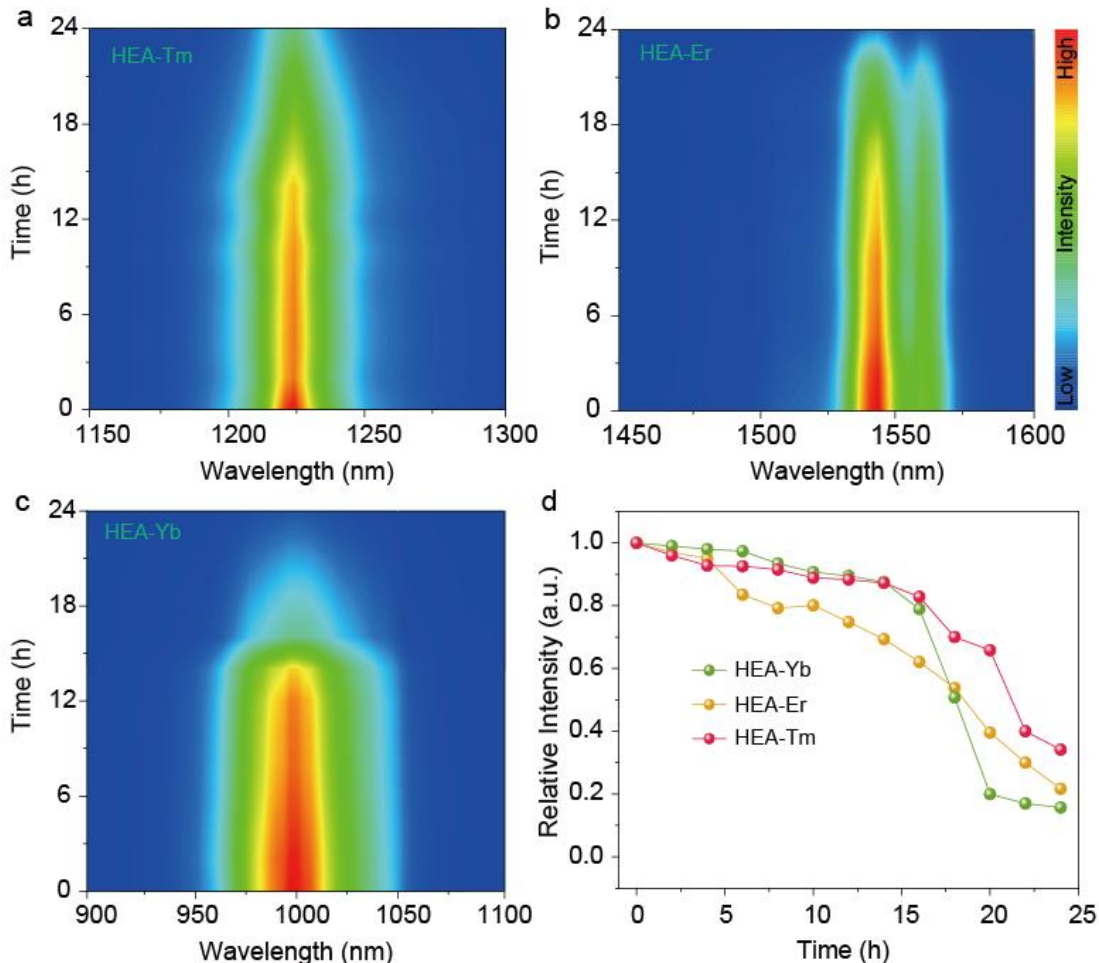


Figure S25. Humidity stability tests (100% RH, 25°C) from 0 to 24 h. NIR PL spectra of HEA-Tm (a), HEA-Er (b) and HEA-Yb (c) single crystals; (d) Time-dependent PL intensity of HEA-Tm, HEA-Er and HEA-Yb single crystals.

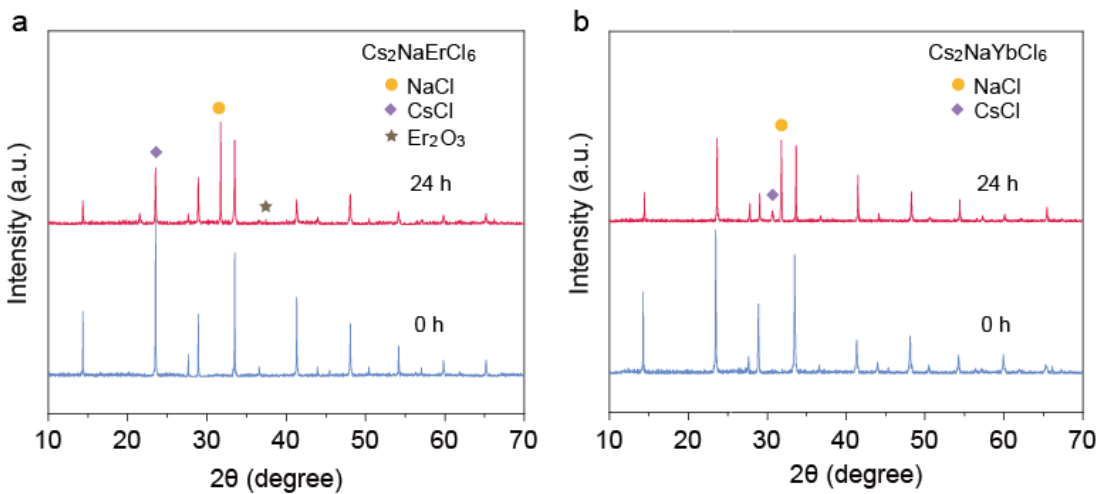


Figure S26. Oxygen stability tests (O_2 , 90%; **50-60% RH**) from 0 to 24 h. XRD of $\text{Cs}_2\text{NaYbCl}_6$ and $\text{Cs}_2\text{NaErCl}_6$ single crystals.

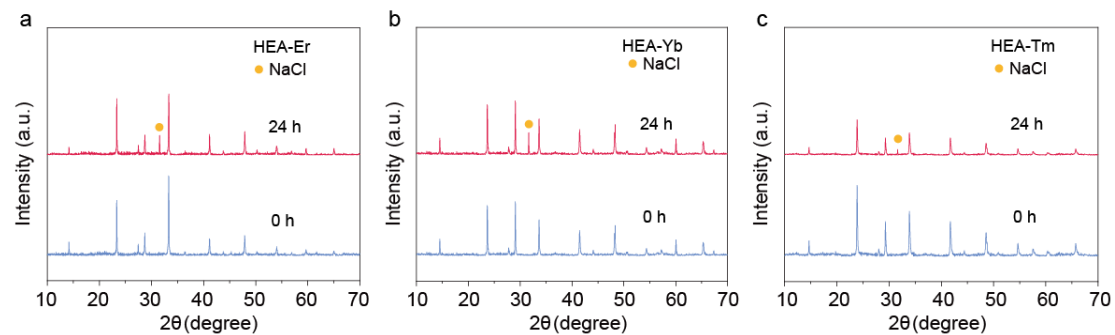


Figure S27. Oxygen stability tests (O_2 , 90%; **50-60% RH**) from 0 to 24 h. XRD of HEA-Er (a), HEA-Yb (b) and HEA-Tm (c) single crystals.

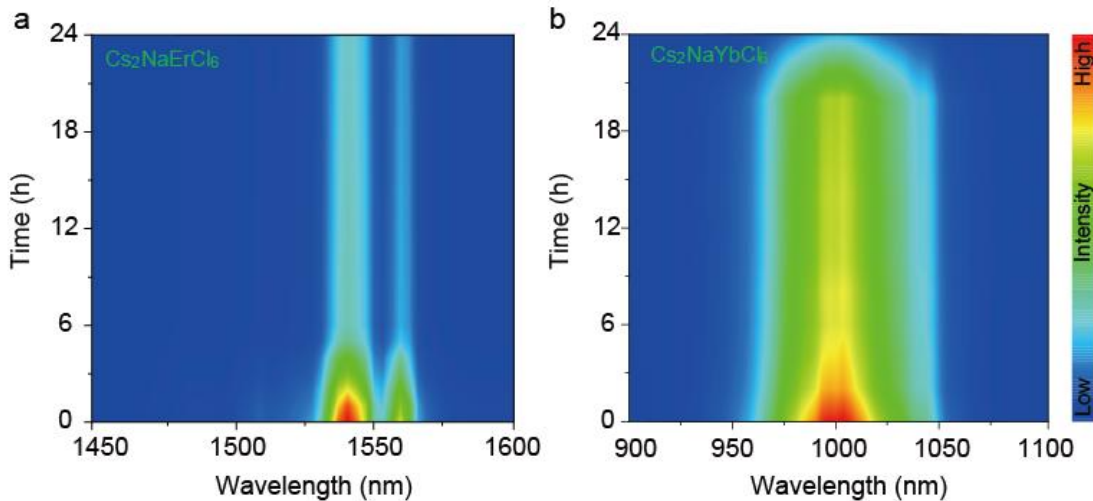


Figure S28. Oxygen stability tests (O_2 , 90%; **50-60% RH**) from 0 to 24 h. NIR PL spectra of $\text{Cs}_2\text{NaErCl}_6$ (a) and $\text{Cs}_2\text{NaYbCl}_6$ (b) single crystals.

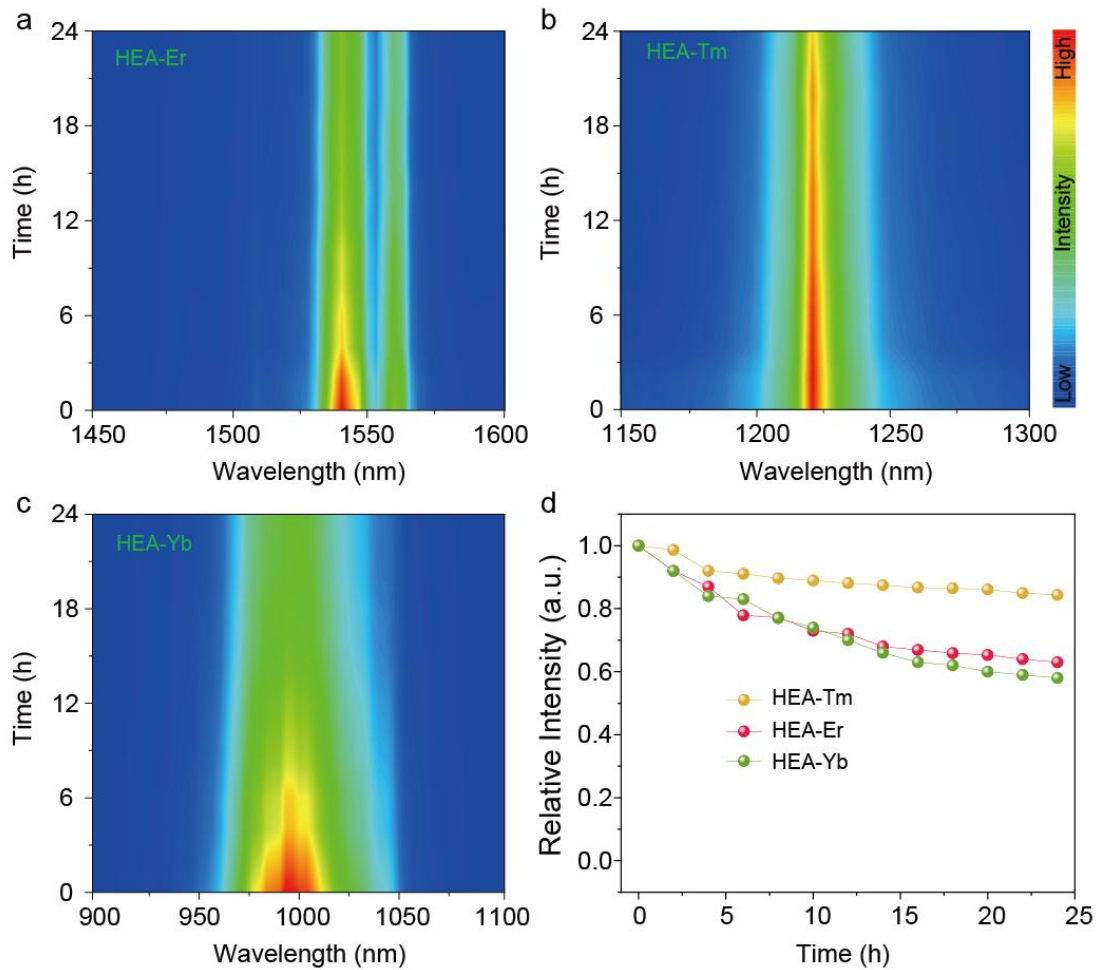


Figure S29. Oxygen stability tests (90%, 50-60% RH) from 0 to 24 h. NIR PL spectra of HEA-Er (a), HEA-Yb (b) and HEA-Tm (c) single crystals; (d) Time-dependent PL intensity of HEA-Tm, HEA-Er and HEA-Yb single crystals.

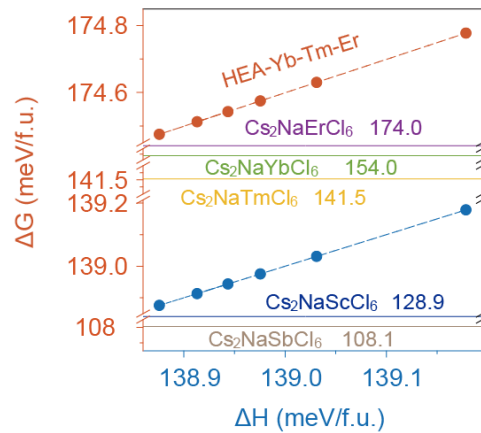


Figure S30. DFT insights into the mechanisms of enhanced environmental stability of HEA-Yb-Tm-Er single crystals. Calculated ΔH (blue line) and ΔG (red line) for HEA-Yb-Tm-Er single crystals; The grey line representing ΔH and ΔG of $\text{Cs}_2\text{NaSbCl}_6$; The

dark red line representing ΔH and ΔG of $\text{Cs}_2\text{NaScCl}_6$; The yellow line representing ΔH and ΔG of $\text{Cs}_2\text{NaYbCl}_6$; The green line representing ΔH and ΔG of $\text{Cs}_2\text{NaTmCl}_6$; The purple line representing ΔH and ΔG of $\text{Cs}_2\text{NaErCl}_6$.

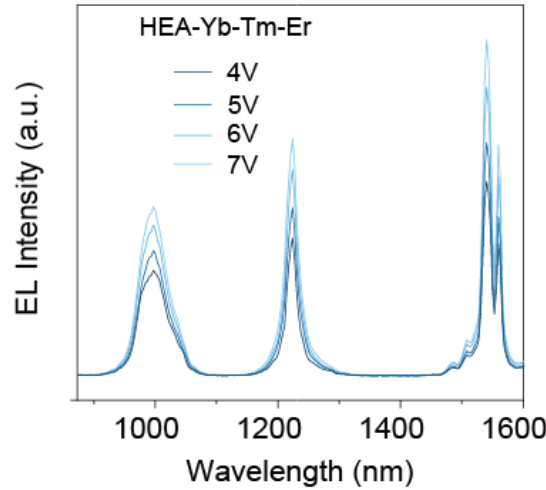


Figure S31. EL spectra for NIR LED based on HEA single crystals under various biases.

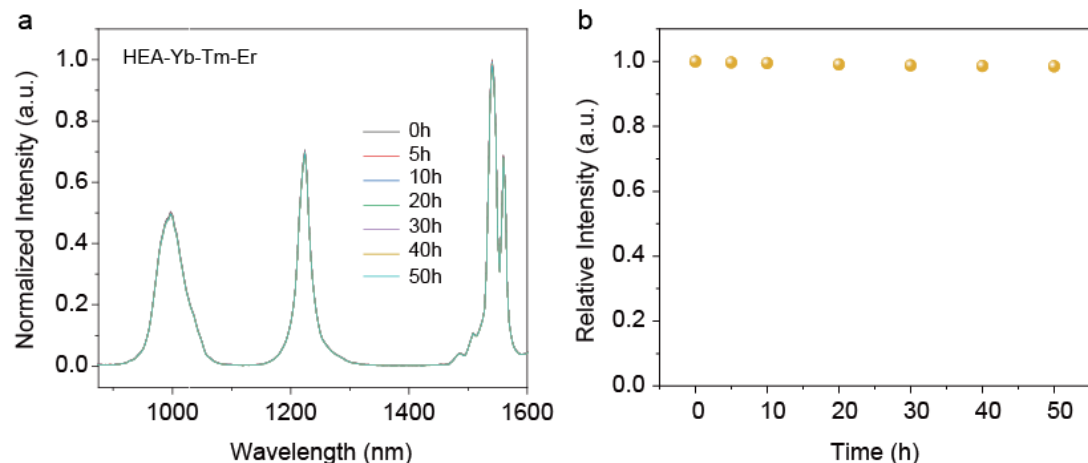


Figure S32. (a) EL spectra of as-fabricated NIR LED based on HEA-Yb-Tm-Er single crystals at different operating time (0-50 h); (b) Time-dependent PL intensity of the NIR LED.

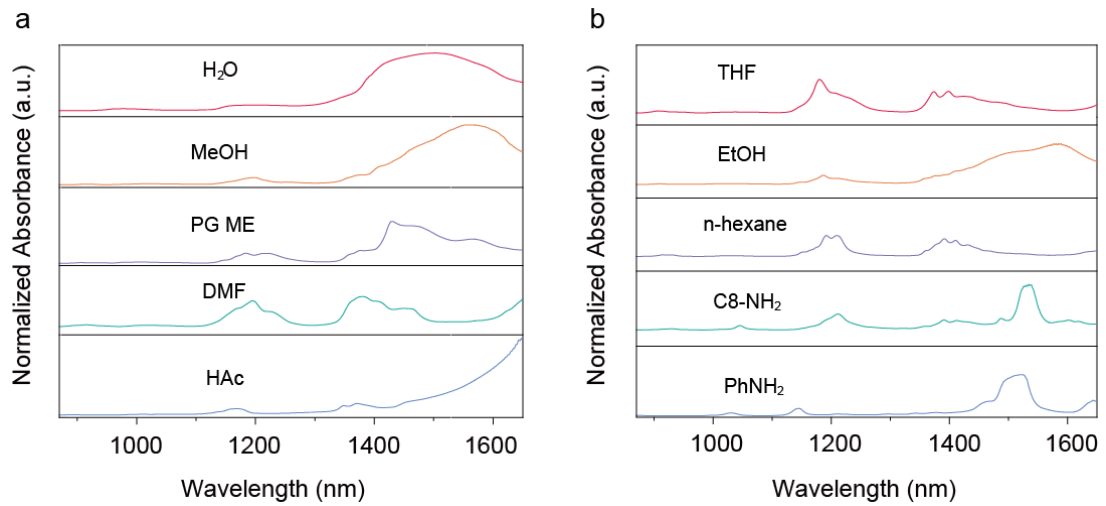


Figure S33. Measured absorption spectra of 10 common solvents

Table S1. Crystallographic parameters obtained from XRD Rietveld refinements for $\text{Cs}_2\text{NaReCl}_6$ ($\text{Re}^{3+} = \text{Sc}^{3+}, \text{Tm}^{3+}, \text{Er}^{3+}$ and Yb^{3+}) and **HEA-Yb-Tm-Er single crystals**.

Sample	Space group	Crystallographic parameters		Reliability factors		
		$a = b = c$ (\AA)	$V(\text{\AA}^3)$	$R_p(\%)$	$R_{wp}(\%)$	$X^2(\%)$
$\text{Cs}_2\text{NaTmCl}_6$		10.6883	1221.029	5.6	8.1	1.07
$\text{Cs}_2\text{NaErCl}_6$		10.7078	1227.724	6.1	9.7	1.12
$\text{Cs}_2\text{NaYbCl}_6$	Cubic	10.6667	1213.641	7.2	9.0	1.36
$\text{Cs}_2\text{NaScCl}_6$	<i>Fm-3m</i>	10.4913	1154.751	3.9	7.5	1.22
HEA-Yb-Tm-Er		10.6073	1193.478	5.3	6.3	1.16

Table S2. Sb and Rare-earth metal content for $\text{Cs}_2\text{NaReCl}_6$ ($\text{Re}^{3+} = \text{Sc}^{3+}, \text{Tm}^{3+}, \text{Er}^{3+}$ and Yb^{3+}) and **HEA-Yb-Tm-Er** studied using Inductively coupled plasma-optical emission spectrometry (ICP-OES).

Samples	Precursor	Product
$\text{Cs}_2\text{NaTmCl}_6$	100	99.32
$\text{Cs}_2\text{NaErCl}_6$	100	99.61
$\text{Cs}_2\text{NaYbCl}_6$	100	99.65
$\text{Cs}_2\text{NaScCl}_6$	100	99.81
(Sb%):HEA-Yb-Tm-Er	20	20.79
(Sc%):HEA-Yb-Tm-Er	20	19.05
(Tm%):HEA-Yb-Tm-Er	20	20.58
(Yb%):HEA-Yb-Tm-Er	20	20.15
(Er%):HEA-Yb-Tm-Er	20	19.43

Table S3. PL decay parameters using bi-exponential fitting of $\text{Cs}_2\text{NaReCl}_6$ ($\text{Re}^{3+} = \text{Sc}^{3+}, \text{Tm}^{3+}, \text{Er}^{3+}$ and Yb^{3+}) and **HEA-Yb-Tm-Er single crystals**.

Sample	τ_1 (ms)	f_1 (%)	τ_2 (ms)	f_2 (%)	τ_{ave} (ms)
$\text{Cs}_2\text{NaTmCl}_6$ (1220 nm)	0.53	16.06	2.97	83.94	2.70
HEA-Tm (1220 nm)	1.37	13.27	3.78	86.73	3.47
HEA-Yb-Tm-Er (1220 nm)	3.73	10.96	7.14	89.04	6.59
$\text{Cs}_2\text{NaYbCl}_6$ (996 nm)	1.17	13.19	2.35	86.81	2.20
HEA-Yb (996 nm)	1.07	13.02	3.50	86.98	3.18
HEA-Yb-Tm-Er (996 nm)	1.24	12.80	4.25	87.20	3.75
$\text{Cs}_2\text{NaErCl}_6$ (1540 nm)	3.15	25.67	13.3	74.33	10.69
HEA-Yb-Tm-Er (1540 nm)	2.54	13.27	15.88	86.73	14.52
HEA-Er (1540 nm)	4.79	10.21	17.9	89.79	15.16